JGR Atmospheres

Key Points:

- Discrepancies found in spatiotemporal variations of volatile organic compounds (VOCs) between field measurements and model simulations
- Anthropogenic VOC emissions in the Pearl River Delta region quantitatively estimated through observations
- Simulations of spatiotemporal variations of VOCs and ozone improved by observation-constrained emissions

Author Contributions:

Conceptualization: Hai Guo
Data curation: Beining Zhou, Yu Wang, Boguang Wang
Formal analysis: Beining Zhou
Funding acquisition: Hai Guo
Investigation: Beining Zhou
Methodology: Beining Zhou, Yangzong Zeren, Xiaopu Lyu, Hongli Wang
Project Administration: Hai Guo
Resources: Hai Guo, Boguang Wang
Supervision: Hai Guo
Validation: Yangzong Zeren, Yu Wang, Hongli Wang
Visualization: Beining Zhou, Yangzong Zeren
Writing – original draft: Beining Zhou
Writing – review & editing: Hai Guo, Xiaopu Lyu, Boguang Wang, Hongli Wang

An Observational Constraint of VOC Emissions for Air Quality Modeling Study in the Pearl River Delta Region

Beining Zhou[1,2] , Hai Guo[1,2] , Yangzong Zeren[1,2], Yu Wang[1,2], Xiaopu Lyu[3], Boguang Wang[4] , and Hongli Wang[5]

[1]Air Quality Studies, Department of Civil and Environmental Engineering, Hong Kong Polytechnic University, Hong Kong, China, [2]Research Institute for Land and Space, Hong Kong Polytechnic University, Hong Kong, China, [3]Department of Geography, Hong Kong Baptist University, Hong Kong, China, [4]Institute for Environmental and Climate Research, Jinan University, Guangzhou, China, [5]State Environmental Protection Key Laboratory of the Cause and Prevention of Urban Air Pollution Complex, Shanghai Academy of Environmental Sciences, Shanghai, China

Abstract Volatile organic compounds (VOCs) have crucial influences on atmospheric chemistry. Accurate quantification of the VOC emissions is critical for air pollution research, especially when applying to air quality models. However, current bottom-up emission inventories have biases, making observational constraints of VOC emissions necessary. We conducted concurrent VOC measurements in the Pearl River Delta (PRD) region during the summer of 2018 and found large discrepancies in the spatiotemporal variations of VOCs between observations and model simulations when using the priori VOC emission inventory (Multi-resolution Emission Inventory for China). The normalized biases of total VOC concentrations ranged from −55% to 85% across the PRD cities in the study period. To improve the simulations, we constrained the anthropogenic VOC emissions based on their measured concentrations. The observation-constrained VOC emissions showed clear diurnal variations and resolved the spatially-concentrated priori emissions by reducing the high emissions by 15%–36% in the central PRD cities while elevating the sparse emissions in other cities. After employing the observation-constrained VOC emissions, the model better reproduced the spatiotemporal variations of VOCs in the PRD region, alleviating the biases to −13%–13%. Furthermore, simulations of peak ozone (O_3) concentrations were amended to reduce the mean normalized bias by 5%–12% on high O_3 days. Our work has effectively combined VOC field measurements with air quality modeling to achieve better simulations of VOCs and O_3. Besides, the observational-constrained emissions are flexible for studying short-term emission changes and their subsequent impacts on air quality.

Plain Language Summary Air quality models are important tools for studying the physical and chemical processes of air pollution. Model simulations rely heavily on the input emission profiles. Despite efforts to establish accurate and model-ready emission inventories, biases persist, which further affects model results. Volatile organic compounds (VOCs) emitted from various anthropogenic sources are key precursors to ozone (O_3) and secondary organic aerosols. In this study, we constructed an observational constraint to validate current VOC emission inventories against observations in nine cities. Constrained emission profiles revealed more pronounced spatiotemporal variations in VOC emissions across cities. Furthermore, since VOC emissions were constrained by observations, air quality model simulations of VOCs and O_3 were significantly improved and more consistent with observations in terms of chemical composition, diurnal variation, and spatial variation. Our proposed approach is efficient and flexible in updating VOC emissions and is suitable for air quality modeling. The improved simulations of VOCs and O_3 provide scientific support for further studies on the impacts of emission changes on air pollution and pollution control strategies.

1. Introduction

Volatile organic compounds (VOCs) play essential roles in atmospheric chemistry as they are the key precursors of secondary air pollutants such as ozone (O_3) and secondary organic aerosol. Ambient VOCs are composed of hundreds of species that are emitted from a wide variety of anthropogenic activities and natural sources, and the contributions of different emission sources varied among regions and cities, corresponding to the distinctive city structures (H. Guo et al., 2017). Therefore, estimations of the VOC emissions are important for investigating air pollution and atmospheric chemistry.

The VOC emission inventories with gridded emissions are necessary inputs for the chemical transport models (CTMs) to study regional air pollution. Current emission inventories of anthropogenic VOC emissions are generated by bottom-up approaches, according to the emission estimations by the annual statistical yearbook on energy consumption and product yields (Huang et al., 2021; F. Liu et al., 2015; J. Zheng et al., 2009b; B. Zheng et al., 2018). However, the limited local measurements of emission factors and the high spatiotemporal variability of the sources have led to difficulties in estimating emissions accurately and timely (Hong et al., 2017; M. Li et al., 2017a; Z. Liu et al., 2012). In addition, the spatial and temporal allocations of VOC emissions from different source sectors (H. Chen et al., 2016; Geng et al., 2017; S. Wang et al., 2011; B. Zheng et al., 2017), along with the speciation of total VOCs into the lumped groups chemical mechanisms (M. Li et al., 2014; Mo et al., 2016), have introduced biases into the model-ready VOC emissions. Consequently, potential errors exist in the emission inventories and could further affect the simulations of VOCs and atmospheric photochemistry in the CTMs.

Discrepancies can be found when applying top-down validations to the model outputs. Recent studies reported that the deviations of simulated and observed VOC concentrations remain even with the latest emission inventories. Shen et al. (2019) reported that the high and increasing anthropogenic VOC emissions dampened the decrease of open fire emissions in parts of China. As a result, the model failed to reproduce the decreasing trend of formaldehyde in these regions. Previous studies also revealed that though the simulated total VOC levels were comparable with those of the observations, biases existed for individual VOC species, such as propane, ethene, toluene, and formaldehyde (Chutia et al., 2019; Jiang et al., 2010; Zeren et al., 2019). In addition, H. Wang et al. (2020) found large differences in the monthly variations of the simulated and observed aromatics in Shanghai, which was caused by the misrepresentation of the monthly emissions. Besides, the discrepancies in the simulated spatiotemporal variations of O_3 concentrations were partially attributable to the biases in emission inventories (Bouarar et al., 2019; Saikawa et al., 2017; X. Wang et al., 2010), especially for the peak values on O_3 pollution days (D. Chen et al., 2013; H. Guo et al., 2019), as well as their spatial distributions (Qu et al., 2020).

In order to better simulate the spatiotemporal variations of VOCs and secondary pollutants, top-down approaches using observed data have been developed to estimate the VOC emissions (B. Li et al., 2021). For example, based on inversion models, satellite observations of formaldehyde and glyoxal have been used to estimate the total VOC emissions, representing the spatiotemporal variabilities of the emissions (Chaliyakunnel et al., 2019; Fu et al., 2007; Z. Liu et al., 2012). Although better simulations of secondary pollutants were achieved using satellite-inversed emissions, the constrained species were limited, and the retrievals for the same species from different satellite instruments have discrepancies (Cao et al., 2018; Stavrakou et al., 2015; R. Zhang et al., 2017). In addition to the satellite observations, field-measured VOCs were applied to constrain the emissions, by using the emission ratios of VOCs relative to an inert tracer (e.g., carbon monoxide and acetylene) (Borbon et al., 2013; Hsu et al., 2010). Meanwhile, the source-receptor relationships, the mixed layer mass balance techniques, as well as the eddy covariance flux measurements were also reliable and complementary for estimating the VOC emissions (Fang et al., 2016; Karl et al., 2007; Mo et al., 2020; Yuan et al., 2015). Studies revealed that after constraining the VOC emissions by measured VOCs, the CTM simulated VOCs and O_3 had better agreement with the observations, particularly for their temporal variations, compared with the simulations without constraints (S. P. Chen et al., 2010; Kim et al., 2011; H. Wang et al., 2020). In spite that frameworks for top-down constraints of VOC emissions with measured data have been established, they suffered from low spatial coverage, and a limited number of them were applicable to input into CTMs. Moreover, due to the lack of concurrent VOC measurements, the uses of observational constraints to estimate VOC emissions were scarce in China, whereas the VOC emissions changed rapidly under fast developments and strengthened control strategies. Therefore, top-down VOC emission constraints in China are necessary for complementing VOC emission assessments and enhancing the CTM simulations of VOCs and secondary pollutants.

The Pearl River Delta (PRD) region is one of the most prosperous city clusters in China. The rapid developments were accompanied by unprecedented VOC emissions, leading to severe air pollution in this region. Since the early 2000s, studies based on field measurements and bottom-up emission inventories have been conducted to characterize the VOC emission sources and O_3 formation chemistry in the PRD region (H. Guo et al., 2006; Huang et al., 2021; Y. Liu et al., 2008; X. Liu et al., 2021; Q. Lu et al., 2013; J. Zheng et al., 2009a). However, no observational constraints of VOC emissions with measured data have been applied to air quality modeling studies to date. This study proposes an updated approach for constraining the anthropogenic VOC emissions by combining concurrent VOC measurements in nine PRD cities and Community Multiscale Air Quality Modeling System (CMAQ) simulations. Then, the CMAQ simulations using both priori and posteriori emissions were

assessed. This study is a new attempt to employ the field measurements of VOCs in CTM simulations in the PRD region to improve simulations of VOCs and secondary pollutants for further studying atmospheric chemistry. In addition, the proposed observational constraint is applicable to future studies on short-term emission changes.

2. Materials and Methods

2.1. Sampling Sites

In this study, concurrent field measurements were carried out in the PRD region during the summer of 2018. The sampling sites covered nine mainland cities, that is, Dongguan (DG), Foshan (FS), Guangzhou (GZ), Huizhou (HZ), Jiangmen (JM), Shenzhen (SZ), Zhuhai (ZH), Zhaoqing (ZQ), and Zhongshan (ZS). One typical urban site of each city was selected for VOC samplings. The sampling sites were located in the residential and commercial areas within the central circles of each city (within a radius of 5–10 km from the city center). There were no industrial factories or highways nearby, and the sites were far from boulevards. As a result, the instantaneous emissions from industries and vehicles were rare. In addition, one suburban site, Conghua (GZ-CH), was also chosen in a suburban town in the northern PRD region. Figure S1 and Table S1 in Supporting Information S1 show the geographical locations of the sampling sites. The samplings were set up in open and high locations (the rooftops of buildings, about 20 m above the ground) without tall buildings and/or trees blocking the air exchanges. Therefore, the samples collected relatively well-mixed air masses representative of urban and suburban environments.

2.2. Field Measurements

Offline VOCs samples were collected in the sampling campaigns at 10 sampling sites. The 1-hr whole air samples were collected using electro-polished stainless-steel SUMMA canisters with valves to ensure that the canisters were filled gradually within 1 hr. The samples were collected at 08:00, 12:00, and 16:00 in local time (LT), and the sampling days were selected based on the weather forecast and analyses of the synoptic systems so that days with heavy rains were avoided. Details of the sampling dates and the number of valid samples collected are listed in Table S1 in Supporting Information S1. The VOC species were identified and quantified by the gas chromatography (GC) coupled with a mass spectrometer detector (MSD), electron capture detector (ECD), and flame ionization detector (FID). Two sets of GC units were connected to MSD/ECD and FID, respectively. In the GC-MSD/ECD system, 250 mL of air from the canister sample was injected into a pre-concentrator and separated into two pathways to enter MSD and ECD, respectively. In the GC-FID system, the 250 mL air sample was concentrated and injected into the FID for chemical analysis of C_2-C_3 VOCs. The determination of VOCs followed the United States Environmental Protection Agency (U.S. EPA) TO-15 method (U.S. EPA, 1999), and Table S2 in Supporting Information S1 lists the limit of detection, precision, and accuracy of each VOC species. In total, 60 VOCs were quantified, including 27 alkanes, 18 alkenes, 1 alkyne, and 14 aromatics. Moreover, regular inter-laboratory comparisons of VOCs analysis have been performed with the Rowland-Blake group at the University of California, Irvine (Blake et al., 2003; Simpson et al., 2010). Reasonably good agreements were achieved for the analysis results between the two laboratories, with the goodness of fit (R^2) values between 0.85–0.97 and slopes close to 1.0 (i.e., 0.85–1.24) for different species, indicating good reliability and quality of the data.

In addition to the offline VOC measurements, hourly VOC concentrations were continuously measured at an urban site in DG (online-U) and a suburban site in JM (online-B) (Table S1 in Supporting Information S1) by the online gas chromatograph-mass spectrometer (GC-MS/866, Chromatotec). The instrument quantified 56 VOC species and was calibrated weekly during the sampling periods. The R^2 values were greater than 0.98 for the calibration curves between the standard gas concentrations and the instrumental response signal, and the limits of detection ranged from 0.02 to 0.35 ppbv for the VOC species. Details about the online GC-MS measurements can be found in Qi et al. (2021). From the online VOC measurements, the monthly average diurnal variations of VOC species were obtained at both urban and suburban sites during summertime, which were used for model evaluations and the calculation of the VOC emission constraint. Note that 51 out of the 56 VOCs measured online were included in the 60 VOCs measured offline. Hence, 50 of them were selected and used in the observational constraint of anthropogenic VOC emissions (Table S2 in Supporting Information S1) according to their abundance, reactivity, and sources. The 50 VOC species were then mapped to eight VOCs in the Carbon Bond

chemical mechanism (CB05) listed in Table S3 in Supporting Information S1 for further calculations and model evaluations by the CMAQ model.

The concentrations of criteria air pollutants in the PRD region were continuously measured throughout the research periods by the China National Environmental Monitoring Center (CNEMC). The data quality assurance and quality control (QA/QC) strictly followed the China National Environmental Protection Standard (CNEMC, 2013). The O_3 and nitrogen dioxide (NO_2) concentrations at 56 environmental monitoring stations (Table S4 in Supporting Information S1) were obtained, among which 10 stations that are close to the VOC sampling sites were used for the statistical evaluations of the model simulations and the observational constraint calculations.

Besides, ground-level meteorological parameters, including temperature, relative humidity, wind speed, and wind direction at Guangzhou Baiyun international airport during June 2018 were obtained from the Integrated Surface Database (NOAA, 2001). The hourly meteorological parameters at the district monitoring stations near the VOC sampling sites were also acquired from the Guangdong Meteorological Bureau. The observed meteorological data were collected for assessing the model simulations and calculating the observation-constrained VOC emission profiles.

2.3. Model Description and Configuration

In this study, the Weather Research and Forecast (WRF v4.0) model and the Community Multiscale Air Quality Modeling System (CMAQ v5.0.2) were applied to simulate the weather and atmospheric chemistry. The WRF model, developed by the National Center for Atmospheric Research along with other collaborators, can produce simulations based on actual atmospheric conditions (Skamarock et al., 2019). The CMAQ model established by the U.S. EPA is compatible with the WRF model and provides fast and technically sound estimations of airborne gases and particles (Binkowski & Roselle, 2003). The WRF-CMAQ model has been widely applied to study regional-scale air quality and is confirmed to be robust in modeling O_3 pollution in previous studies (Jiang et al., 2010; N. Wang et al., 2015; H. Wang et al., 2018).

In this study, the simulations were performed for the whole month of June 2018 with a prior 24-hr spin-up. As shown in Figure S2 in Supporting Information S1, three nested domains were employed for the WRF model with a spatial resolution of 3 km for the innermost domain, covering the PRD region. The same domains were set in the CMAQ model but with one grid cell being cut from each side of the domain. The vertical levels were set to 51 sigma levels with the model top at 50 hPa in the WRF simulations, while the layers were compressed to 15 layers in the CMAQ model with approximately 7 layers inside the boundary layer. Details about the physical and chemical schemes utilized in the models are listed in Table S5 in Supporting Information S1. The WRF model was driven by the Final (FNL) Operational Global Analysis data with a spatial resolution of $1° \times 1°$ and a time interval of 6-hr (NCEP et al., 2000). Meanwhile, the land cover type from the Moderate Resolution Imaging Spectroradiometer (MODIS) Land Cover Type Product (MCD12C1) Version 6 (Friedl & Sulla-Menashe, 2015) at $0.05° \times 0.05°$ spatial resolution was applied to update the land use in WRF simulations. As for the CMAQ simulations, the Model of Emissions of Gases and Aerosols from Nature (MEGAN v2.04) (Guenther et al., 2006) was used to derive the biogenic emissions. In addition, the priori anthropogenic emissions were based on the 2017 Multi-resolution Emission Inventory for China (MEIC) (M. Li et al., 2017a; B. Zheng et al., 2018) and the 2010 Asian emission inventory (MIX) (M. Li et al., 2017b) within and outside mainland China respectively. Note that the priori anthropogenic emission inventories (grid resolution at $0.25° \times 0.25°$) were applied to the base model simulation, while in the constrained model simulation, the anthropogenic VOC emissions in the PRD region were updated by the observation-constrained emissions (posteriori emissions).

2.4. Model Performance

The mathematical statistics, including the mean bias (BIAS), root mean square error (RMSE), correlation coefficient (COE), and index of agreement (IOA), were applied to evaluate the model performance based on the observations. Overall, the WRF model captured the dominant weather systems over East Asia (d01) during the simulation period (Figure S3 in Supporting Information S1), and the meteorological fields in the PRD region were reproduced. Table S6 in Supporting Information S1 lists the values of the evaluation statistics for meteorological parameters at district monitoring stations in the PRD cities. The surface temperature and relative humidity were well simulated in all cities, indicated by good correlations (COE ranged from 0.73–0.89 and 0.76–0.85, respectively) and good agreements (IOA ranged from 0.78–0.92 and 0.79–0.90 respectively). The positive mean bias

(0.65–1.65 m/s) reflected that the surface wind speeds were slightly overestimated. Such biases in the simulated wind speed using the WRF model have been commonly reported in previous studies (M. Li et al., 2016; Matsui et al., 2009), which can be attributed to the deficiency in the rough terrains adopted in the model. Despite that, the agreements between the simulated and observed wind speeds were within a reliable range (0.56–0.80), and the RMSE values lay in the benchmark of 2 m/s (Emery et al., 2001). In addition, the time series of the simulated and observed meteorological parameters at Guangzhou International Airport presented in Figure S4 in Supporting Information S1 further depicts that the simulations matched the observations. Discrepancies were mainly found on days influenced by tropical cyclones (5–9 June) and the outskirt of the Western Pacific Subtropical High-Pressure system (20–26 June), which had unstable atmospheric conditions with precipitations and strong surface winds. The complexity of the unstable atmosphere has made it difficult to perform good simulations by WRF (Kumar et al., 2012). Nonetheless, the simulated wind directions were consistent with those observed, indicating that the simulations of surface wind fields were reliable. Furthermore, the model represented the temperature gradients and captured the strongly mixed vertical wind profiles in the planetary boundary layer (Figure S5 in Supporting Information S1), enhancing the credibility of the simulation of boundary layer dynamics.

The overall good performance in simulating the meteorological fields by the WRF model has provided confidence in the simulations of chemical fields by the CMAQ model. As shown in Figure S6 and Table S7 in Supporting Information S1, the simulations of O_3 concentrations in the PRD cities agreed well with the observations. The COE values ranged from 0.56 to 0.82, above the projected benchmark of 0.5 (Emery et al., 2017), and the IOA values were between 0.74 and 0.86. Moreover, the statistics of simulated O_x (O_3 + NO_2) (Table S8 in Supporting Information S1), which has eliminated the effects of the conversion between O_3 and nitrogen oxides (NO_x), were better than those of O_3, indicating reasonable simulations of the chemical fields. However, discrepancies between simulated and observed O_3 concentrations remain, related to uncertainties in emission inputs of O_3 precursors (i.e., VOCs and NO_x), biases in rough urban terrain (Jiménez et al., 2010), and limitations in the model presentation of complex urban dynamics (Cuchiara et al., 2014; Y. Zhang et al., 2013) and photochemical reactions (Mar et al., 2016; Tuccella et al., 2012). Even though the modeled O_3 concentrations in the constrained model simulation were generally comparable with those in the base model simulation (Figure S6 in Supporting Information S1), the O_3 levels on high O_3 days were better represented. The improvements of simulated O_3 using observation-constrained anthropogenic VOC emissions will be further discussed in the following section.

2.5. Calculation of the Observational Constraint

The calculation of observational constraint was based on the Eulerian Box Model according to the mass conservation of a species inside a fixed box (Seinfeld & Pandis, 2006). In the Eulerian box, the atmosphere in the area of interest is assumed to be well-mixed, and the concentration of a species is determined by its emission, chemical reactions, removal (dry and wet depositions), horizontal transport, and vertical dilution. Each PRD city, except for GZ, where GZ-U and GZ-CH were treated separately, was regarded as a three-dimensional box. Thereby, the mass-balanced rate of change with time (t) for the concentration of species (i) within the box of volume ($L \cdot W \cdot H(t)$) can be calculated via Equations 1a and 1b as follow:

$$\frac{dc_i}{dt} = \frac{q_i}{H(t)} - R_i - \frac{s_i}{H(t)} + \frac{c_i^0 - c_i}{\tau_r} \quad \text{for } \frac{dH(t)}{dt} \leq 0 \tag{1a}$$

$$\frac{dc_i}{dt} = \frac{q_i}{H(t)} - R_i - \frac{s_i}{H(t)} + \frac{c_i^0 - c_i}{\tau_r} + \frac{\left(c_i^a - c_i\right)}{H(t)} \frac{dH(t)}{dt} \quad \text{for } \frac{dH(t)}{dt} > 0 \tag{1b}$$

where i represents CB05 VOCs; c_i (molecules $\cdot$ cm^{-3}) is the concentration of VOC$_i$; q_i (molecules $\cdot$ cm^{-2} $\cdot$ s^{-1}) is the mass emission rate of VOC$_i$, $H(t)$ (cm) is the planetary boundary layer height (PBLH); R_i (molecules $\cdot$ cm^{-3} $\cdot$ s^{-1}) is the chemical loss rate of VOC$_i$; s_i (molecules $\cdot$ cm^{-3} $\cdot$ s^{-1}) is the removal rate of VOC$_i$; c_i^0 (molecules $\cdot$ cm^{-3}) is the background concentration of VOC$_i$; τ_r (s) is the residence time of air in the box; c_i^a (molecules $\cdot$ cm^{-3}) is the concentration of VOC$_i$ above the PBL.

Furthermore, Equations 1a and 1b can be rearranged to solve for the VOC emission rate (q_i), yielding Equations 2a and 2b:

$$q_i = \frac{dc_i}{dt} H(t) + R_i H(t) + s_i - \frac{c_i^0 - c_i}{\tau_r} H(t) \quad \text{for } \frac{dH(t)}{dt} \leq 0 \tag{2a}$$

$$q_i = \frac{dc_i}{dt}H(t) + R_iH(t) + s_i - \frac{c_i^0 - c_i}{\tau_r}H(t) - \left(c_i^a - c_i\right)\frac{dH(t)}{dt} \quad \text{for } \frac{dH(t)}{dt} > 0 \tag{2b}$$

The constraint calculation employed both field measurements and base model simulation. The offline measured VOC concentrations at each site and the online measured diurnal variations of VOCs were used, along with the measured O_3 concentrations and meteorological parameters. In addition, the WRF-CMAQ simulations of the hydroxyl (OH) radical and nitrate (NO_3) radical concentrations, as well as the PBLH were applied to the calculation. Details for estimating each term in Equations 2a and 2b are discussed in the following sections. After constraint calculation, daily emission profiles of CB05 VOC species in each city, including GZ-U and GZ-CH, were obtained. The gridded emissions in the priori emission inventory at each city point were then replaced by the observation-constrained emissions. Thereby, spatially distributed diurnal VOC emissions for the PRD region, which are ready for input into the CTMs, are achieved. Finally, the observation-constrained VOC emission profile was inputted into the CMAQ model for the constrained simulation, and the outputs were evaluated.

2.5.1. VOC Concentrations in the City "Box," (c_i)

The measured VOCs at each site were assumed to be representative of each city (including GZ-U and GZ-CH), according to the sampling site selection (Table S1 in Supporting Information S1). Therefore, the averaged VOC concentrations at each site were used in the calculation of each city and district. Meanwhile, the change rate of VOC concentrations ($\frac{dc_i}{dt}$) was derived from the measured diurnal variations of each VOC. The derivative was calculated by the central difference in numerical differentiation. As shown in Equation 3, the VOC concentration at time t ($c_{i,t}$) was determined by that at the former ($c_{i,t-1}$) and later ($c_{i,t+1}$) time points, where the time interval (Δt) was 1 hr.

$$\frac{dc_{i,t}}{dt} = \frac{c_{i,t-1} - c_{i,t+1}}{2\Delta t} \tag{3}$$

2.5.2. Chemical Loss of VOCs, (R_i)

Ambient VOCs are actively involved in photochemical reactions, where the VOCs are oxidized by OH radical, O_3, and NO_3 radical (T. Wang et al., 2017). During the daytime, OH radical initiates the oxidation of VOCs, promoting O_3 formation (Atkinson & Arey, 2003; Taccone et al., 2016), while nighttime oxidation by either O_3 or NO_3 removes VOCs, especially alkenes (Brown et al., 2011; H. Wang et al., 2018; Warneke et al., 2004). Therefore, the chemical loss of VOCs (R_i) via reactions with OH radical, O_3, and NO_3 radical were estimated in Equation 4:

$$R_i = k_{OH,i}c_{OH}c_i + k_{O_3,i}c_{O_3}c_i + k_{NO_3,i}c_{NO_3}c_i \tag{4}$$

where k is the reaction rate constant of oxidants with individual VOC ($cm^3 \cdot molecules^{-1} \cdot s^{-1}$); c is the concentration of oxidants and VOCs ($molecules \cdot cm^{-3}$).

The reaction rate constants (k_{OH}, k_{O_3}, and k_{NO_3}) for each VOC were obtained from the CB05 mechanism (Yarwood et al., 2005) and calculated according to the observed temperature in each city. Meanwhile, observed O_3 concentrations at each site, as well as the model-derived OH and NO_3 concentrations, were adopted in the calculation due to the lack of direct measurements of the radical concentrations (K. Lu et al., 2018). As discussed in Text S1 in Supporting Information S1, the CMAQ model has reproduced the diurnal variations of OH and NO_3 concentrations, and the peak values were comparable with those reported in previous studies in the PRD region. Therefore, based on the rational results, the model-derived OH and NO_3 concentrations were applicable to the calculation.

2.5.3. Removal of VOCs, (s_i)

Dry deposition is important in removing gaseous pollutants (Enrico et al., 2016; Seinfeld & Pandis, 2006). The dry deposition flux is usually calculated by Equation 5, where the dry deposition velocity ($v_{d,i}$, $cm \cdot s^{-1}$) was determined by the nature of the depositing surface and the chemical properties of the depositing species (Wesely, 1989). Existing gaseous dry deposition schemes considered inorganic gases, including sulfur dioxide, O_3, and a small number of organic compounds (L. Zhang et al., 2023). Most of these organic species are oxygenated VOCs (OVOCs) such as carbonyls, acids, and peroxides, which were efficiently deposited by vegetation stomatal uptake or by the effective Henry's law partitioning onto moist surfaces (Karl et al., 2010; Nguyen et al., 2015; Wu et al., 2021). However, the OVOC species were not measured in this study, while little information

is available on the dry deposition of VOC species other than OVOCs (Goldstein & Galbally, 2007), especially in the urban environment, where the dry deposition loss is very weak due to the large resistance in barren and urban land use (L. Zhang et al., 2002, 2003). Thus, the dry deposition of VOCs was not considered in estimating the observation-constrained VOC emissions.

$$s_i = v_{d,i} c_i \tag{5}$$

2.5.4. Horizontal Transport of VOCs Out of the City "Box," (T)

The contributions of horizontal transport to VOC concentrations within the box (T) are determined by the residence time (τ_r, s) and the background VOC concentrations (c_i^0, molecules $\cdot$ cm^{-3}), as presented in Equation 6a, where positive and negative values represent the horizontal transport of VOCs out of and into the box, respectively.

$$T = -\frac{c_i^0 - c_i}{\tau_r} H(t) \tag{6a}$$

$$\tau_r = \frac{L}{u} \tag{6b}$$

The residence time (τ_r) of air in the area (Equation 6b) was expected to be the ratio of the length of each city box in the prevailing wind direction (L, cm) to the average observed wind speed (u, cm/s). According to Figure S8 in Supporting Information S1, southerly and easterly winds prevailed in most PRD cities during the study period, except for GZ-U, where north winds accounted for relatively high percentages. Hence, the box length (L) for each city is estimated based on the south-north and west-east length of the minimum envelope for the administrative area of each city. The calculated residence time ranged from 4 to 12 hr. Besides, the minimum VOC concentrations measured at the suburban site (GZ-CH) were used as the background concentrations in the calculation.

2.5.5. Vertical Dilution of VOCs in the City "Box," (E)

The planetary boundary layer evolves with time as a result of the heat transfer between the surface and atmosphere, which leads to vigorous vertical mixing of the air (Holzworth, 1967). Generally, the PBLH varies diurnally, with low values during the nighttime and higher values during the daytime. The developments of PBLH have great impacts on the concentrations of air pollutants by modulating the box volume and entraining the air above PBL. Physically, when the PBLH decreases ($\frac{dH(t)}{dt} \leq 0$), there is no direct change in the concentration inside the box, as the air originally inside the box is left aloft above the box (Seinfeld & Pandis, 2006). However, when the PBLH increases ($\frac{dH(t)}{dt} > 0$), the box entrains air from the layer above, the free troposphere, where the concentrations of most air pollutants were considerably lower than those in the PBL. Subsequently, this entrainment will dilute the emitted pollutants inside the box. Thus, the entrainment of the air above PBL was considered when the PBLH increases ($\frac{dH(t)}{dt} > 0$).

The vertical dilution rate of the entrainment (E) was calculated by Equation 7a, considering the differences between the VOC concentrations aloft (c_i^a) and inside (c_i) the box, as well as the change rate of PBLH ($\frac{dH(t)}{dt}$). As the VOCs were mainly emitted from sources inside the PBL, the concentrations of VOCs above the PBL (c_i^a) were thereby assumed to be zero for all VOCs.

$$E = -\left(c_i^a - c_i\right) \frac{dH(t)}{dt} \tag{7a}$$

$$\frac{dH(t)}{dt} = \frac{H_{t-1} - H_{t+1}}{2\Delta t} \tag{7b}$$

The mean PBLH in each city and district was extracted from the WRF simulations, as there were no available measurements during the sampling campaign. The PBLH were generally well-simulated with clear diurnal patterns (Figure S9 in Supporting Information S1), and the daily maximum heights were in line with the recorded seasonal average of 800–1000 m during summertime (J. Guo et al., 2016). Besides, the change rate of the PBLH ($\frac{dH(t)}{dt}$) was calculated by the numerical differentiation of the PBLH at former and later time points (Equation 7b).
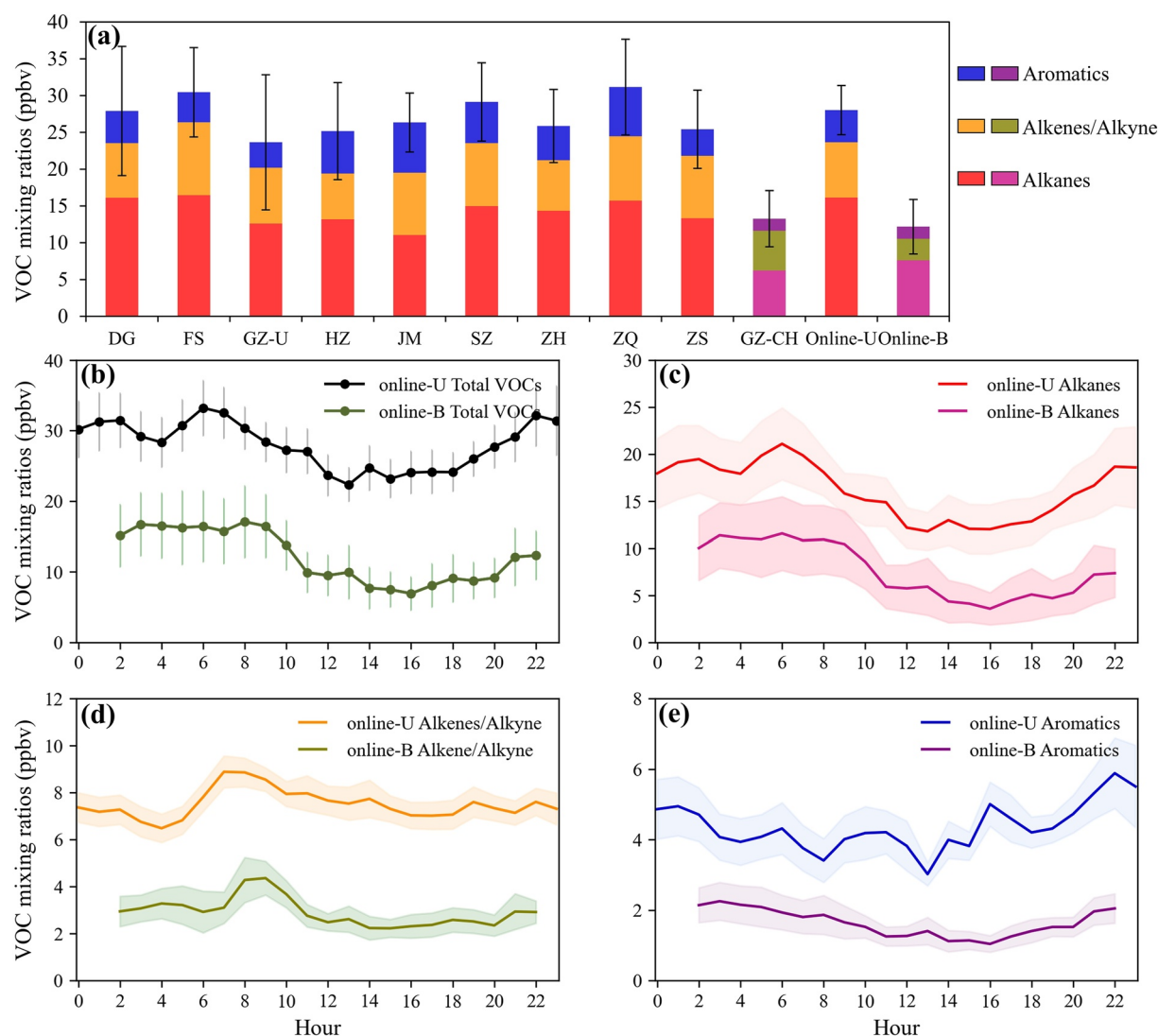
Figure 1. (a) Average volatile organic compound (VOC) concentrations (ppbv) at 10 sampling sites measured offline and two sites measured online (online-U and online-B). (b–e) Monthly average diurnal variations of total VOC concentrations and VOC groups (ppbv) measured online. The total VOCs and VOC groups refer to the 50 constrained VOC species listed in Table S2 in Supporting Information S1 and 3 biogenic VOCs (isoprene, α-pinene, and β-pinene). The error bars and the shaded areas present the standard deviations of the total VOC concentrations and the concentrations of VOC groups, respectively.

3. Results and Discussion

3.1. Overview of the Field Measurements

During the study period (June 2018), the PRD region was under the impact of the summer monsoon and tropical cyclones, which were representative of presenting typical summertime weather conditions in South China. The measured total VOC concentrations varied among different areas, as shown in Figure 1a. In urban areas, ZQ and FS had the highest total VOC concentrations (31.16 ± 6.51 ppbv and 30.46 ± 6.07 ppbv, respectively), followed by SZ (29.14 ± 5.32 ppbv) and DG (28.05 ± 8.78 ppbv). The total VOC concentrations in the other urban areas were around 23–26 ppbv, nearly double that in the suburban site GZ-CH (13.27 ± 3.82 ppbv). The higher VOC concentrations in urban areas than that in the suburban areas were mainly due to the more intensive anthropogenic VOC emissions, such as vehicular emissions, which were found to be the major VOC sources in the PRD region (H. Guo et al., 2011, 2017). In addition to the spatial distributions of total VOC concentrations, the compositions of VOC groups in different areas were also different. Among the three VOC groups, alkanes accounted for the largest percentage of total VOC concentrations at all sites (41.94%–57.46%), consistent with previous studies in the PRD region (He et al., 2019; Meng et al., 2022; Zou et al., 2015). Meanwhile, the proportions of alkenes

and alkyne (24.70%–40.85%) were higher than those of aromatics (12.30%–25.90%). The higher contribution of alkenes and alkyne to the total VOC concentrations in GZ-CH (40.85%) than in the urban areas (24.70%–33.38%) was attributable to the weaker anthropogenic emissions of alkanes and alkenes and relatively stronger biogenic emissions of isoprene in the suburban areas (Tang et al., 2007). Besides, aromatics, mainly evaporated from volatile solvents (H. Guo et al., 2007; Y. Zhang et al., 2013), had different contributions to the total VOC concentrations among cities, with higher proportions in JM (25.90%), HZ (22.87%), and ZQ (21.45%). The spatial variations of VOC compositions in the PRD region were related to the different emission sources among cities (Louie et al., 2013; Yuan et al., 2012).

Furthermore, online VOCs observations were carried out at urban and suburban sites (online-U and online-B), and the concentrations of VOCs were consistent with those at the 10 offline sampling sites (Figure 1a). Figures 1b–1e illustrate the monthly averaged diurnal variations of VOC concentrations at online-U and online-B. The VOC concentrations were found to have similar daily patterns in both urban and suburban areas, with slight increases in the early morning and significant decreases from noon to afternoon, under the influences of emissions, photochemical reactions, and vertical mixing. During the daytime, both anthropogenic activities and biogenic emissions were enhanced, while the photochemical reactions were boosted, and the vertical mixing of air was facilitated by the evolution of the planetary boundary layer, leading to decreases in VOC concentrations in the afternoon (An et al., 2014; K. Li et al., 2019; Wei et al., 2018; Zou et al., 2015).

The field measurements showed that the total VOC concentrations and VOC compositions in the PRD region had noticeable spatiotemporal variations, corresponding to the different VOC emissions characteristics among cities and areas. Given the intensive anthropogenic activities in this region, VOCs were mainly emitted from anthropogenic sources (Barletta et al., 2005; Bian et al., 2019; Y. Liu et al., 2008). Therefore, this study only focused on anthropogenic VOCs.

3.2. Base Model Simulation

Before constraining the anthropogenic VOC emissions, the priori emission inventory was used as input for the base model simulation. Figure 2a illustrates the spatial distributions of the total CB05 VOC concentrations (i.e., the sum of eight CB05 VOC species listed in Table S3 in Supporting Information S1) in the PRD region from field measurements and base model simulation. The measured total CB05 VOC concentrations were in the range of 60–80 ppbv in urban areas and around 30 ppbv in suburban areas. Although the base model simulation has generally reproduced the higher VOC concentrations in the central PRD region than those in the suburban and rural areas around, the simulated VOC concentrations were overestimated at SZ (113.11 ± 37.61 ppbv), GZ-U (110.77 ± 26.50 ppbv), and FS (104.96 ± 28.06 ppbv) by 39%–85%. Meanwhile, the simulated VOC concentrations in western PRD cities, including ZQ (44.22 ± 24.21 ppbv), JM (42.57 ± 15.76 ppbv), and ZH (36.19 ± 15.46 ppbv), were underestimated by -32% to -55%. As shown in Figure 2c, high anthropogenic VOC emissions were allocated to SZ, FS, and GZ-U in the priori emission inventory, whereas ZQ, JM, and ZH had rather low VOC emissions. It was found that the simulated VOC concentrations were highly related to the input anthropogenic VOC emissions in the CMAQ model. Hence, constraining the anthropogenic VOC emissions based on field measurements in each city would be beneficial for better simulating the VOC concentrations.

In addition to the total CB05 VOC concentrations, the VOC compositions had essential influences on atmospheric photochemistry, as the reactivity of VOCs with oxidants varied among species. For instance, alkenes with olefinic carbon bonds (ETH, OLE, and IOLE) are more reactive than alkanes with only paraffinic carbon bonds (ETHA and PAR) (Atkinson, 1997), while the concentration of PAR is proportionally greater than that of other groups because it lumps more VOC species. Aromatics (BENZENE, TOL, and XYL) are grouped according to the number of alkyls, with XYL having polyalkyl, such as xylenes, being more reactive than other aromatics (Atkinson, 1986). Due to the different emission characteristics of VOC sources, the compositions of VOCs were inconsistent among the PRD cities. Thus, the reactivity of CB05 VOC species with OH radical, which initiates the oxidation of VOCs, from field measurements and the base model simulation were compared in Figure 3. In line with the spatial distributions of total CB05 VOC concentrations, the simulated total OH reactivity from the base model was much higher in SZ (9.85 ± 2.87 s^{-1}), GZ-U (8.86 ± 2.64 s^{-1}), and FS (8.69 ± 2.31 s^{-1}) and much lower in ZQ (2.79 ± 0.59 s^{-1}), JM (2.83 ± 0.58 s^{-1}) and ZH (2.76 ± 0.57 s^{-1}), compared with the measured OH reactivity in the PRD cities, which was within the range of 4.78–6.45 s^{-1}. Though the simulated total CB05 VOC concentrations in DG (72.81 ± 39.85 ppbv) and HZ (59.16 ± 26.32 ppbv) were close to the
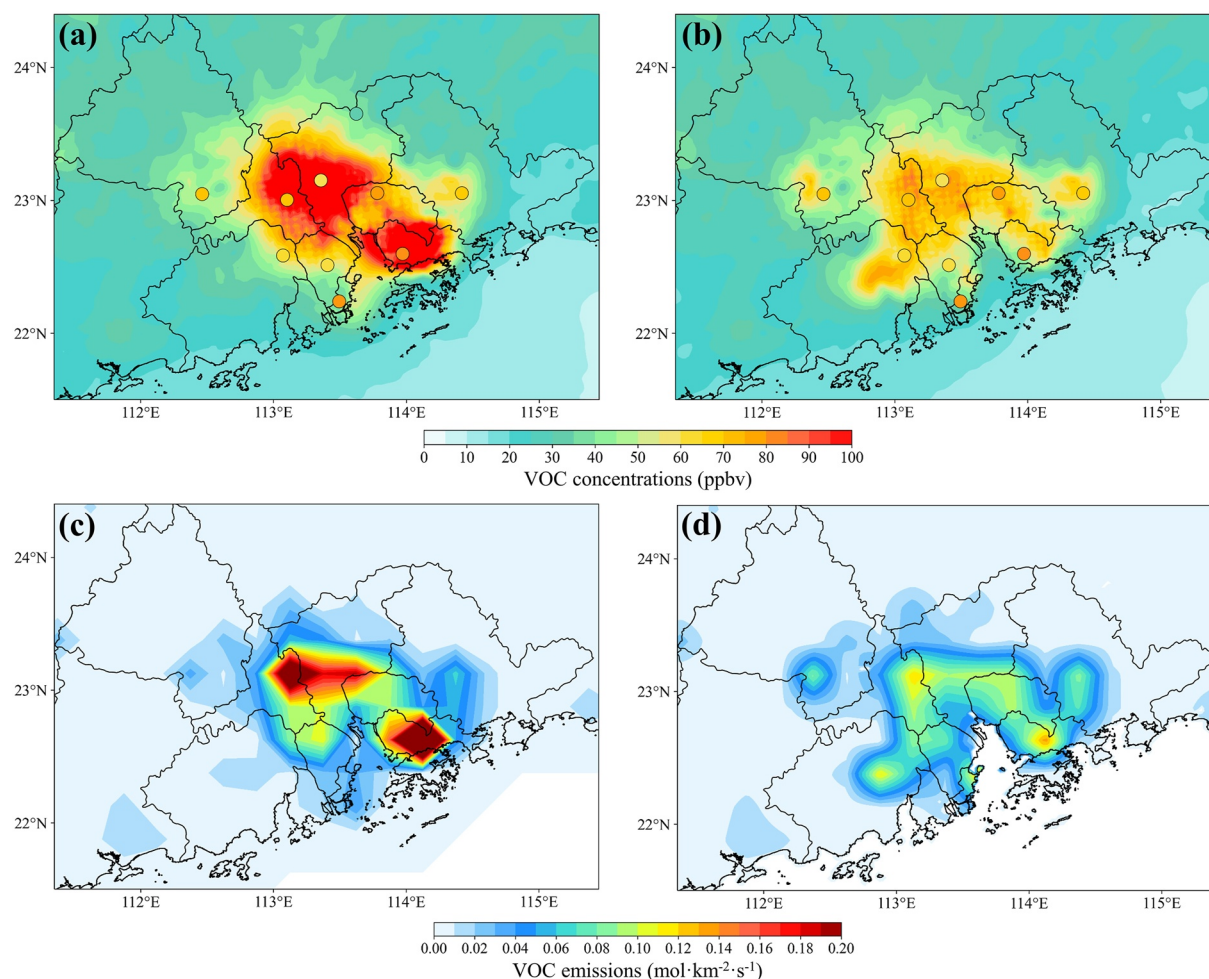
Figure 2. (a and b) Average total CB05 volatile organic compound (VOC) concentrations (sum of eight CB05 VOC species listed in Table S3 in Supporting Information S1) throughout the study period (ppbv). (a) Base model simulation; (b) constrained model simulation. The contour colors represent the model simulations; scatter points are the field measurements. (c and d) Monthly average total CB05 VOC emissions (mol · km^{-2} · s^{-1}). (c) VOC emissions in priori emission inventory. (d) Observation-constrained VOC emissions.

observations (78.60 ± 39.25 ppbv and 69.11 ± 33.01 ppbv, respectively), discrepancies were still found in the simulations of OH reactivity, with higher total OH reactivity in DG (base simulation: 6.64 ± 1.96 s^{-1}; measurement: 4.97 ± 0.60 s^{-1}) and lower in HZ (base simulation: 3.34 ± 0.86 s^{-1}; measurement: 5.65 ± 0.71 s^{-1}). Apart from that, differences were also found in the contributions of individual VOC species to the total OH reactivity, especially for the species that have rather low concentrations but high reactivity. The model overestimated the proportion of IOLE (base simulation: 9.41%–21.71%; measurement: 4.15%–9.24%), while the contributions of XYL (base simulation: 14.03%–17.62%; measurement: 17.74%–38.11%) were underestimated. These discrepancies further indicated that there were large biases in the simulations of VOC compositions. Therefore, it is necessary to constrain the emissions of individual VOCs separately in order to better reproduce the VOC compositions in each city.

As for the temporal variations of VOC concentrations, Figure 4a presents the monthly average diurnal patterns of total CB05 VOC concentrations from the base model simulation at each city and the observations at online-U and online-B. It was clear that the base model simulation reproduced the general decrease of VOC concentrations around noon, relating to the boosted photochemical reactions and the increased boundary layer height. However, the prominent peaks in the early morning and the evening were unrealistic compared to the relatively gentle changes in the field measurements. More specifically, the diurnal variations of measured VOCs varied among species in different areas are illustrated in Figure S10 in Supporting Information S1. Slight increases in the early morning and decreases during daytime were observed at both urban and suburban sites for PAR, ETHA, ETH,
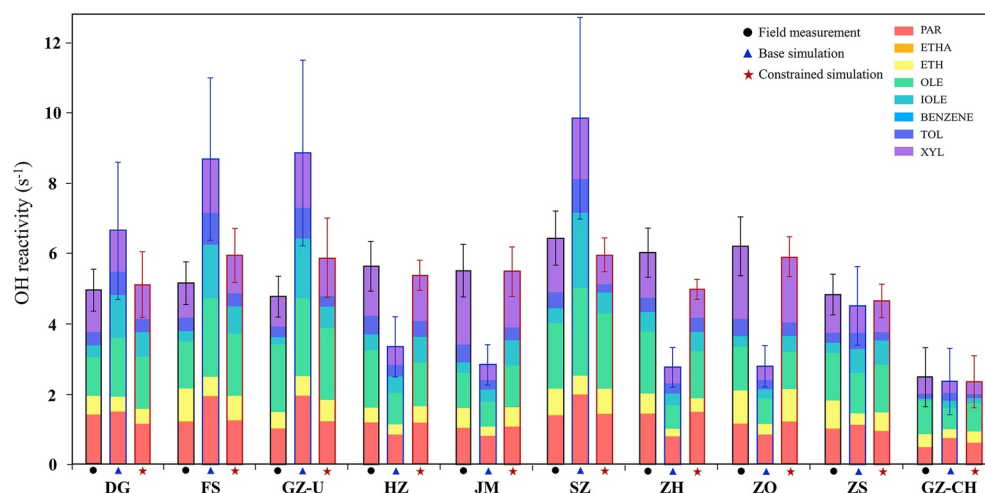
Figure 3. Average OH reactivity (s^{-1})* of CB05 volatile organic compound (VOC) species at 10 sampling sites. The black circle, blue triangle, and red star denote the field measurements, base model simulation, and constrained model simulation, respectively. The error bars represent the standard deviations. *OH reactivity = $k_i \times$ [VOC]$_i$, where k_i represents the reaction rate constant of each CB05 VOC species with OH radical; [VOC]$_i$ represents the concentration of each CB05 VOC species.

and OLE, while the aromatics species showed different patterns in urban and suburban areas. For example, the concentrations of BENZENE increased during the daytime, and the levels of TOL and XYL varied throughout the day in urban areas. However, the simulated VOCs had similar diurnal patterns for all CB05 VOC species in each city. Hence, discrepancies between the simulated and observed VOCs were mainly found during the daytime. Given the biases in both spatial distributions and diurnal variations of simulated VOCs, the observational constraint of VOC emissions was applied in this study to improve the simulations of VOCs by the CMAQ model.

3.3. Observation-Constrained VOC Emissions

By applying the observational constraint in Section 2.5, diurnal emission profiles of each anthropogenic VOC species in different cities can be obtained. As shown in Figure 5, the VOC emissions had clear diurnal patterns in the urban areas with more intensive emissions in the daytime, whereas the emissions in suburban areas were relatively low with insignificant diurnal variations. In order to estimate the VOC emissions in each city, the locally-emitted VOCs removed by chemical consumption, horizontal transport, and vertical dilution were calculated according to Equations 4 and 7. Specifically, horizontal transport out of the city had the highest contributions to the total VOC emissions, accounting for 73.36%–89.71% in urban areas and 57.95% in suburban areas. The contributions of horizontal transports were associated with the wind speeds in different cities, which were higher in ZH (4.04 ± 2.19 m/s) and lower in GZ-CH (1.69 ± 1.03 m/s). In comparison, vertical dilution and
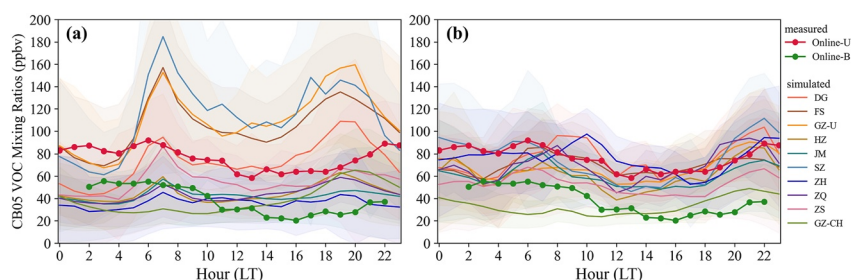

Figure 4. Monthly average diurnal variations of total CB05 volatile organic compound (VOC) concentrations at each site (ppbv). The red and green curves are the measured data at online-U and online-B, respectively; the other lines are the model simulations with standard deviations shown in shaded areas. (a) The base model simulation; (b) The constrained model simulation.
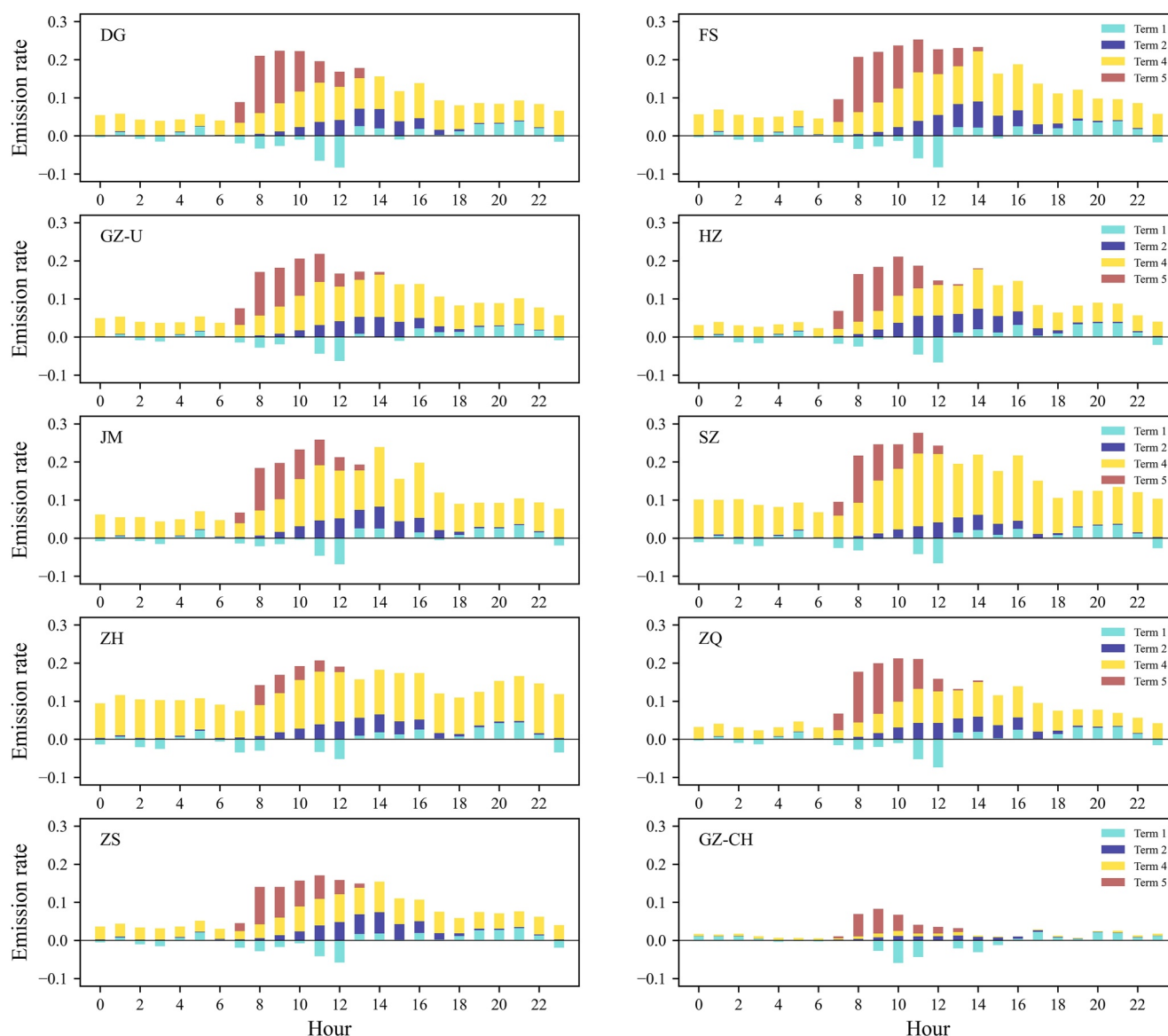
Figure 5. Observation-constrained total CB05 volatile organic compound (VOC) emission profiles in each city and district. The colors represent different terms in the calculation (Equations 2a and 2b), where Term 1 is the change rate of VOC concentrations; Term 2 is the chemical loss rate; Term 3 is the removal rate, which was not considered in the calculation in Section 2.5.3; Term 4 is the horizontal transport rate; Term 5 is the vertical dilution rate. Unit: $mol \cdot km^{-2} \cdot s^{-1}$.

chemical consumption mainly contributed during the daytime. The vertical dilution was strong in the morning (8:00–10:00 LT) when the boundary layer rises (Figure S9 in Supporting Information S1), and gradually weakened until early afternoon (13:00–14:00 LT) when the PBLH reached its daily maximum. The PBLH in each city also affects the intensity of vertical dilution, and as the PBLH values were derived from WRF simulation, the accompanying uncertainty was analyzed in Section 3.5. Similarly, the chemical reactions of VOCs were boosted during noon-time (11:00–14:00 LT), corresponding to the enhancement of solar radiation and OH radical concentrations (Figure S7a in Supporting Information S1). The calculated chemical loss of VOCs was dominated by OH-initiated oxidations, accounting for 86.67%–90.95% of the total chemical loss in all cities and districts on average. Meanwhile, the chemical loss of alkenes via reactions with O_3 and NO_3 was found to be significant at night, with mean contributions of 8.44%–12.12% and 0.21%–1.21%, respectively. The significant oxidation reaction with OH radical was, therefore, a dominant loss mechanism of VOCs (de Gouw et al., 2017; Parrish et al., 2007). Given that the model simulated OH concentrations were employed in the calculations, the biases of the simulations could result in uncertainties, which were further estimated in Section 3.5. Besides, the VOC
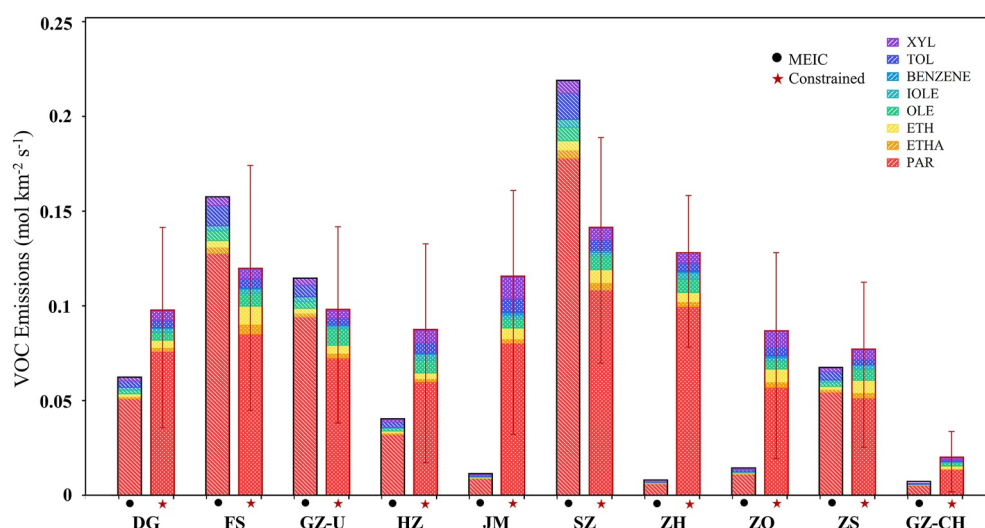
Figure 6. Daily average CB05 volatile organic compound (VOC) emissions (mol · km^{-2} · s^{-1}) in each city and district. The black circle and red star denote the 2017-based Multi-resolution Emission Inventory for China (MEIC) emission and the observation-constrained emissions, respectively. The error bars represent the standard deviations.

change rates (Equation 3) were used to offset the VOC emissions related to processes that were not considered in the calculation (Equations 4 and 7). The impacts of the VOC change rates on the total VOC emissions were considerably smaller than the abovementioned three terms (i.e., horizontal transport rate, vertical dilution rate, and chemical loss rate), with negative contributions around noon (11:00–12:00 LT), which led to slight decreases in VOC emissions. Overall, the diurnal variations of anthropogenic VOC emissions were associated with human activities when emissions from vehicles, industries, etc., were mainly recorded during the daytime.

The daily average VOC emission rates from the priori emission inventory and the observational constraint are presented in Figure 6. In the priori emission inventory, the total anthropogenic VOC emissions were mainly concentrated in SZ (0.22 mol · km^{-2} · s^{-1}), FS (0.16 mol · km^{-2} · s^{-1}), and GZ (0.12 mol · km^{-2} · s^{-1}). In contrast, the emissions in ZQ, JM, and ZH were noticeably low, less than 0.02 mol · km^{-2} · s^{-1}. In comparison, the observation-constrained emissions in SZ, FS, and GZ-U were reduced by 15%–36% to 0.14 ± 0.05, 0.12 ± 0.06, and 0.10 ± 0.05 mol · km^{-2} · s^{-1}, respectively, while the anthropogenic VOC emissions in other cities were enhanced after the observational constraint. In particular, the total VOC emissions in JM, ZH, and ZQ were substantially elevated from 0.012, 0.007, and 0.014 to 0.12 ± 0.06, 0.13 ± 0.04, and 0.09 ± 0.05 mol · km^{-2} · s^{-1}, respectively. Table S9 in Supporting Information S1 compares the emissions of each VOC species in priori and posteriori emission profiles, showing that the magnitudes of the emission correction varied for each city due to different emission characteristics of VOC species across cities. It is worth noting that, in addition to incorporating BENZENE emissions into the constrained profiles, the emission intensities of VOC species did not necessarily increase or decrease with the increase or decrease of total VOC emissions. Specifically, the reductions in the total VOC emissions in FS and GZ-U mainly resulted from the reduced emissions of PAR, TOL, and IOLE, while the emissions of ethane (ETHA), ethene (ETH), OLE, and XYL raised after the constraints. Furthermore, although the total VOC emissions in ZS showed the smallest increase among cities (by 14%), the compositions of VOC emissions changed with the decreases of PAR and TOL and the increases of other species, especially alkenes (ETH, OLE, and IOLE). The above results suggest that observation-constrained emissions not only corrected the levels of total VOC emissions in the priori emission inventory but also modulated the proportions of VOC species in the emission profiles, which would affect the simulations of VOC compositions and O$_3$ photochemistry in the CMAQ model. The observation-constrained VOC emission profiles for the different VOC species in each city and district were then interpolated into the model grids using the spatial distribution factors within each city. Accordingly, the spatially-distributed posteriori anthropogenic VOC emissions in the PRD region were obtained (Figure 2d) with more accordant emissions distributed in the urban areas of each city than the priori emissions (Figure 2c).

The updates in the diurnal variations and spatial allocations of anthropogenic VOC emissions after the observational constraint have better represented the VOC emission characteristics in the urban areas of the PRD region.

Thereby, with the observation-constrained VOC emissions, the performance of the CMAQ model simulation for the VOCs in the PRD cities would be further enhanced compared with that of the base model simulation.

3.4. Constrained Model Simulation

The observation-constrained anthropogenic VOC emissions herein were used to drive the CMAQ model again for the constrained model simulation. Figure 2b shows that the total VOC concentrations from the constrained model simulation were in agreement with the field measurements, as the normalized biases between simulated and observed average total VOC concentrations across cities dropped from $-55\%–85\%$ to $-13\%–13\%$ in the simulation period. The modeled VOC levels were higher in urban areas (53.29–76.57 ppbv) and lower in the suburban area GZ-CH (33.19 $\pm$ 17.33 ppbv). Compared with the base model simulation (Figure 2a), the unexpectedly high VOC concentrations in SZ, GZ-U, and FS decreased substantially by 33%–39% in the constrained simulation, while the relatively high VOCs observed in urban ZQ and JM were reproduced. In terms of the VOC compositions, the model better simulated the OH reactivity of VOCs after the observational constraint (Figure 3). The modeled monthly average OH reactivity in urban areas varied from 4.66 to 5.98 s^{-1}, within the measured range of 4.78–6.45 s^{-1}. Besides, the modeled reactive VOC species in the constrained simulation were more comparable with the field measurements. In particular, the contributions of ETH and XYL to the total OH reactivity were enhanced to 7.58%–15.54% and 14.05%–31.60%, respectively, in the constrained simulation. Similar levels were found in observed ETH and XYL with contributions of 7.30%–17.93% and 17.74%–38.11%, respectively. The proportions of IOLE with constraint were reduced to 7.48%–14.71%, comparable to the measurement (4.15%–9.24%). As a result, the CMAQ simulations better represented the spatial distributions of the VOC concentrations and compositions in the PRD region after applying the observation-constrained VOC emissions.

The diurnal variations of simulated VOCs were more consistent with those measured after observational constraint (Figure 4b), which had small peaks in the morning and evening, accompanied by considerable troughs in early afternoon. Moreover, the simulated VOCs presented different diurnal patterns among species, as shown in Figure S11 in Supporting Information S1. For PAR, ETHA, ETH, and OLE, the increases in the morning and decreases around noon were well-reproduced by the constrained model simulation in different cities. The model also captured the different patterns for aromatics species (i.e., BENZENE, TOL, and XYL) in urban and suburban areas. Hence, benefiting from the diurnal emission profiles after observational constraint, the CMAQ model could better reveal the temporal variations of VOCs in the PRD region.

Furthermore, the modeled O_3 concentrations were well-improved on O_3 pollution days (Figure S6 in Supporting Information S1), especially on 11 June, when 40 out of 56 environmental monitoring stations recorded daily maximum O_3 concentrations over 100 ppbv, the Grade II standard of China's national air quality. The high-pressure system on 11 June (Figure S12 in Supporting Information S1) provided favorable weather conditions for photochemical reactions with intense solar radiation and high temperature, prompting the O_3 formation. Figure 7 shows the spatial distribution of simulated and observed O_3 concentrations during this O_3 pollution event. The base model simulation overestimated the O_3 levels, with the mean normalized bias (MNB) of 17% between observed and simulated O_3. Meanwhile, the 95th percentile of modeled O_3 concentrations across the innermost domain (d03) reached 147.98 ppbv in FS and offshore areas. The overestimation was in accordance with the high chemical production rates of O_3 in these areas. As key O_3 precursors, the abundance and compositions of VOCs modulate the O_3 productions. Therefore, with the improved simulations of VOCs using observation-constrained VOC emissions (Figure 2d), the CMAQ model was able to simulate the O_3 photochemistry better. In the constrained simulation, the modeled O_3 chemical production rates were alleviated in FS and the offshore areas while slightly enhanced in JM. Consequently, the modeled O_3 concentrations were amended, as the MNB value decreased to 12%, and the 95th percentile of O_3 concentrations in d03 also reduced by 10% to 133.46 ppbv. Thereafter, the pivot area of high O_3 levels moved to the western PRD region and the estuary. Similar improvements were found on 29 June, when O_3 concentrations in the eastern PRD region were relatively high (Figure S13 in Supporting Information S1). By using observation-constrained VOC emissions, the simulation of O_3 was greatly improved, reducing the MNB value from 30% to 18%, and the 95th percentile by 8%. In addition, the O_3 hotspot in GZ and HZ was mitigated as a result of the eased O_3 chemical production. The reduced biases between simulation and observation after constraining the VOC emissions reflect that the CMAQ model performed better in simulating the spatial distributions of O_3 concentrations on high O_3 days.

In spite of the improvements in high-level O_3 concentrations during O_3 pollution events, the modeled O_3 concentrations on days without extreme O_3 pollution were comparable between constrained and base model simulations (Figure S6 in Supporting Information S1) because the concentrations of O_3 were influenced by meteorological
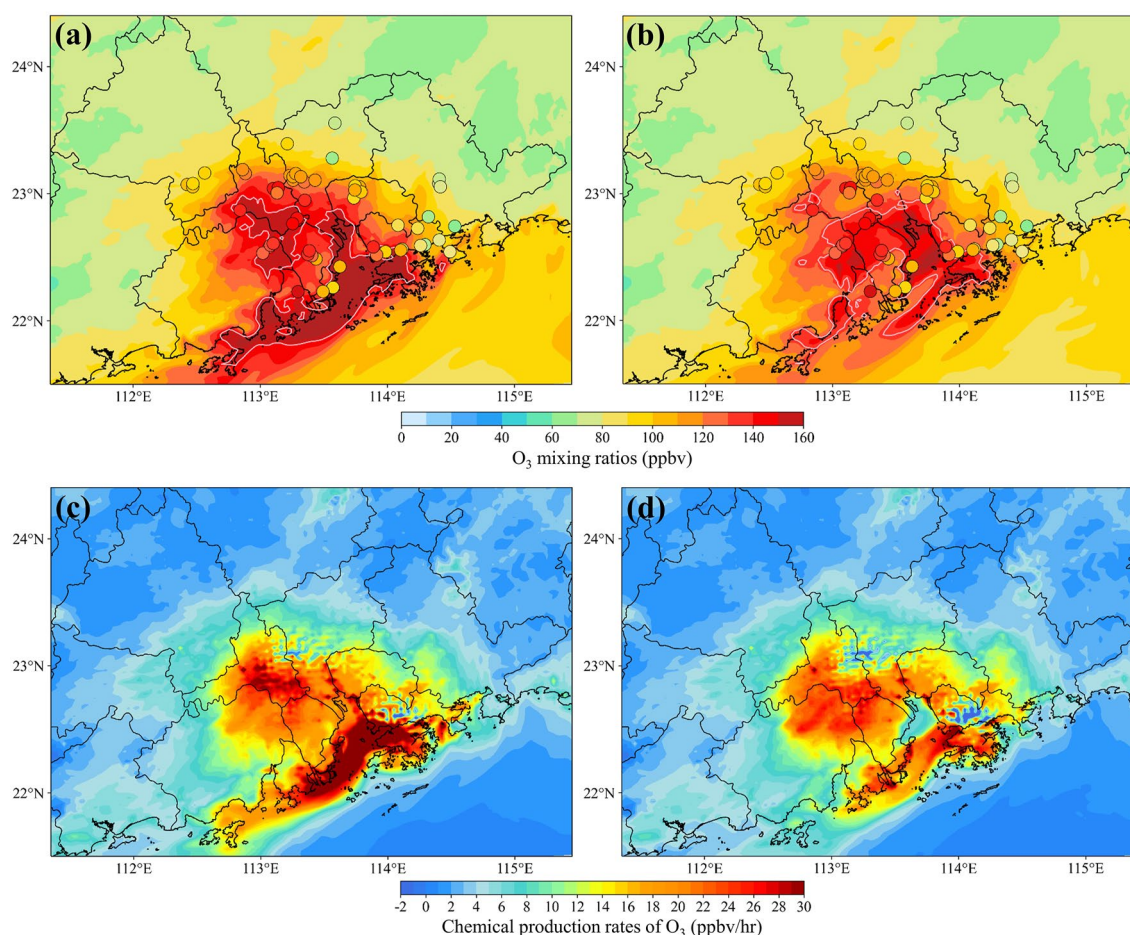
Figure 7. (a) Ground-level O$_3$ concentrations (ppbv) on 11 June 2018 at 14:00 local time (LT) from the base model simulation (background color) and observations (colored circles). (b) Same as (a) but for modeled O$_3$ concentrations (ppbv) from constrained model simulation. The pink contour line refers to the 95th percentile of O$_3$ concentrations in d03, which was 147.98 ppbv in the (a) base model simulation and 133.46 ppbv in (b) constrained model simulation. The O$_3$ monitoring stations are listed in Table S4 in Supporting Information S1. (c and d) Modeled chemical production rates of O$_3$ (ppbv/hr) on 11 June 2018 at 14:00 LT from the (c) base model simulation and (d) constrained model simulation.

conditions and photochemical reactions (Y. Liu & Wang, 2020a, 2020b). Moreover, due to the non-linearity of O$_3$-persour relationships, both VOCs and NO$_x$ levels impact regional O$_3$ pollution (H. Lu et al., 2019). Hence, insignificant differences in simulated O$_3$ concentrations between the constrained and base model simulations were found in lower-level O$_3$ concentrations. The remaining discrepancies in simulations and observations were the combined results of complex urban dynamics and O$_3$ photochemistry, which might not be fully captured by WRF and CMAQ models.

Overall, constraining the anthropogenic VOC emissions by observations has led to better model simulations of VOCs and O$_3$. The abundance and compositions of modeled VOCs in each city were improved, achieving better representations of the spatial distributions and diurnal variations of VOCs in the PRD region. Moreover, the enhanced VOC simulations facilitated the simulations of O$_3$ photochemistry. The high O$_3$ concentrations on O$_3$ pollution days were then well-reproduced by the CMAQ model, which would be beneficial for further studying regional O$_3$ pollution.

3.5. Uncertainty Analysis

In the calculation of observational constraint, model-derived radical concentrations and PBLH in the PRD cities were applied due to the lack of direct measurements. Although the modeled OH concentrations and PBLH were within reasonable ranges compared with previous field measurements, as discussed in Section 2.5 and Text S1

in Supporting Information S1, the biases of simulated values would introduce uncertainties into the calculated emission profiles. Therefore, the Monte Carlo framework (Text S2 in Supporting Information S1) was applied to quantify the propagation of uncertainties in the observation-constrained emissions. In addition, the box length was determined by the size of the minimum envelope covering the administrative area of each city and might vary when using different measurement methods. Hence, the sensitivity of the calculated emissions to different box lengths was also estimated using a Monte Carlo framework. Given that SZ has the highest VOC emission rates among the PRD cities in both the priori emission inventory and observation-constrained emissions, the uncertainty analysis for SZ was selected as a representative of the observation-constrained emissions in the PRD region. The daily maximum OH concentrations observed in urban SZ, ranging from $2–9 \times 10^6$ molecules $\cdot$ cm^{-3} (Yang et al., 2022), were employed in the Monte Carlo runs. The noon-time PBLH was set to the range of 600–1200 m, according to the measured PBLH in Guangdong province during summer (J. Guo et al., 2016). As for the city's box length, it ranged from half to twice the original city length. The input parameters (i.e., OH concentrations, PBLH, and box lengths) were randomly sampled from the pre-defined ranges, and then the Monte Carlo simulations were repeated 10,000 times.

The Monte Carlo runs yielded the probability distributions of estimated emissions, which statistically assessed the uncertainties corresponding to each input parameter. In the simulations for OH concentrations (Figure S14a in Supporting Information S1), the total CB05 VOC emissions had an average of 0.140 mol $\cdot$ km$^{-2} \cdot$ s^{-1} under the 5th–95th percentiles of 0.135–0.146 mol $\cdot$ km$^{-2} \cdot$ s^{-1}. Accordingly, the estimated uncertainties in the total VOC emissions based on the mean value were between −3.97% and 3.80%. Meanwhile, due to the more significant contributions of the chemical reaction term to the emissions of reactive VOC species, the uncertainties for OLE, IOLE, and XYL were relatively larger, reaching ±18% to ±23%. In terms of the PBLH simulations, the 5th–95th percentiles of the total VOC emissions were 0.117–0.188 mol $\cdot$ km$^{-2} \cdot$ s^{-1}, with the mean value at 0.149 mol $\cdot$ km$^{-2} \cdot$ s^{-1}. Hence, the uncertainties related to the PBLH were between −21.93% and 26.20% (Figure S14b in Supporting Information S1), which were more influential compared with those caused by the OH concentrations. Moreover, Figure S14c in Supporting Information S1 shows that the sensitivity of the total VOC emissions to the city's box length was relatively high, and the deviations from the average emissions (0.145 mol $\cdot$ km$^{-2} \cdot$ s^{-1}) were −25% to 37%. Nonetheless, the levels of the uncertainties herein were much less than those estimated for VOC emission inventories in China, which were over 50% (Huang et al., 2021; M. Li et al., 2017a; H. Liu et al., 2017). Therefore, the uncertainty analysis indicated that the uncertainties brought by the use of model-derived values and the estimations of the city's box length do not substantially impact the validity of the observation-constrained VOC emissions.

4. Conclusion

Estimations of the VOC emissions are important for studying the formation of secondary air pollutants, especially for their applications in air quality models. Although efforts have been made to create accurate VOC emission inventories, biases still exist, which further influence the model simulations of VOCs and secondary pollutants. Hence, in this study, we employed an observational constraint of the anthropogenic VOC emissions based on concurrent field measurements and WRF-CMAQ simulations in the PRD region. The VOCs characteristics of diurnal variations and species compositions in nine PRD cities were investigated through concurrent field measurements in the summer of 2018. Large discrepancies were found between the simulated and observed VOCs, regarding the spatial distributions and temporal variations of the VOCs and their compositions, when using the priori emission inventory. The normalized biases of the average total VOC concentrations across the PRD cities ranged from −55% to 85% during the study period. By applying the observational constraint, diurnal VOC emission profiles in each city were assigned, corresponding to the removal of VOCs by chemical compositions, horizontal transport, and vertical dilution. Instead of concentrating the total anthropogenic VOC emissions in SZ, GZ, and FS in the priori emission inventory, the observation-constrained emissions corrected the spatial allocations of VOC emissions in the urban PRD region. The total VOC emissions in SZ, FS, and GZ-U were reduced by 36%, 24%, and 15%, respectively, while substantially higher emissions were apportioned to ZH, JM, ZQ, DG, and HZ. Therefore, after using the posteriori emissions in the CMAQ model, the normalized biases of the average total VOC concentrations dropped to −13%–13%. The simulated VOC levels were comparable to observations, as the overestimated VOC levels decreased by 33%–39% in SZ, GZ-U, and FS, while the underestimated VOC concentrations increased in ZH, JM, and ZQ. The diurnal VOC emissions also facilitated better simulations of the temporal variations of different VOC species. Furthermore, as VOCs are key precursors to O$_3$, the simulations

of O$_3$ photochemistry were amended so that the high-level O$_3$ concentrations on O$_3$ pollution days were better reproduced. The mean normalized biases between observed and simulated O$_3$ concentrations were reduced by 5%–12%, and the overestimated 95th percentile was abated by 8%–10%.

This work is the first to combine VOC field measurements with CTM modeling studies in the PRD region. The results demonstrate that top-down constraints based on observation can be used to update the VOC emission profiles, which further help to reduce biases in the simulations of VOCs and O$_3$ that the CTMs are suffering from. The improved simulations of VOCs were favorable for further studying atmospheric chemistry, especially O$_3$ photochemistry. More importantly, our observational constraint is flexible to reflect the emission variations in a specific region during a short-term period, in particular, the emission changes due to human interference. For example, the Covid-19 lockdowns, as well as the emission controls in China during the 2008 Summer Olympics in Beijing and the 2016 G20 Summit in Hangzhou. The constrained VOC emissions would better represent the emission characteristics during these periods and assist in air quality studies, providing useful information for air pollution control policies. Meanwhile, limitations remain in this study due to the limited number of sampling sites and period for sampling campaigns. Therefore, future applications of the observational constraint could be expected to have a broader and denser network of sampling locations, as well as continuous measurements for extended periods.

Data Availability Statement

China air quality monitoring data retrieved from the CNEMC is available at (CNEMC, 2018). The WRF model (version 4.0) (Skamarock et al., 2019) and the CMAQ model (version 5.0.2) (U.S. EPA, 2014) were used. The meteorological datasets for the WRF model can be downloaded from (NCEP et al., 2000). The observed meteorological parameters were obtained from the Integrated Surface Database (NOAA, 2001). The MODIS MCD12C1 version 6 data is available at (Friedl & Sulla-Menashe, 2015). We acquired the MEIC and MIX emission inventories from (MEIC, 2017; MIX, 2010).

References

An, J., Zhu, B., Wang, H., Li, Y., Lin, X., & Yang, H. (2014). Characteristics and source apportionment of VOCs measured in an industrial area of Nanjing, Yangtze River Delta, China. *Atmospheric Environment*, *97*, 206–214. https://doi.org/10.1016/j.atmosenv.2014.08.021

Atkinson, R. (1986). Kinetics and mechanisms of the gas-phase reactions of the hydroxyl radical with organic compounds under atmospheric conditions. *Chemical Reviews*, *86*(1), 69–201. https://doi.org/10.1021/cr00071a004

Atkinson, R. (1997). Gas-phase tropospheric chemistry of volatile organic compounds: 1. Alkanes and alkenes. *Journal of Physical and Chemical Reference Data*, *26*(2), 215–290. https://doi.org/10.1063/1.556012

Atkinson, R., & Arey, J. (2003). Gas-phase tropospheric chemistry of biogenic volatile organic compounds: A review. *Atmospheric Environment*, *37*, 197–219. https://doi.org/10.1016/s1352-2310(03)00391-1

Barletta, B., Meinardi, S., Sherwood Rowland, F., Chan, C. Y., Wang, X., Zou, S., et al. (2005). Volatile organic compounds in 43 Chinese cities. *Atmospheric Environment*, *39*(32), 5979–5990. https://doi.org/10.1016/j.atmosenv.2005.06.029

Bian, Y., Huang, Z., Ou, J., Zhong, Z., Xu, Y., Zhang, Z., et al. (2019). Evolution of anthropogenic air pollutant emissions in Guangdong Province, China, from 2006 to 2015. *Atmospheric Chemistry and Physics*, *19*(18), 11701–11719. https://doi.org/10.5194/acp-19-11701-2019

Binkowski, F. S., & Roselle, S. J. (2003). Models-3 Community Multiscale Air Quality (CMAQ) model aerosol component 1. Model description. *Journal of Geophysical Research*, *108*(D6), 4183. https://doi.org/10.1029/2001JD001409

Blake, N. J., Blake, D. R., Simpson, I. J., Meinardi, S., Swanson, A. L., Lopez, J. P., et al. (2003). NMHCs and halocarbons in Asian continental outflow during the Transport and Chemical Evolution over the Pacific (TRACE-P) field campaign: Comparison with PEM-West B. *Journal of Geophysical Research*, *108*(D20), 8806. https://doi.org/10.1029/2002JD003367

Borbon, A., Gilman, J. B., Kuster, W. C., Grand, N., Chevaillier, S., Colomb, A., et al. (2013). Emission ratios of anthropogenic volatile organic compounds in northern mid-latitude megacities: Observations versus emission inventories in Los Angeles and Paris. *Journal of Geophysical Research: Atmospheres*, *118*(4), 2041–2057. https://doi.org/10.1002/jgrd.50059

Bouarar, I., Brasseur, G., Petersen, K., Granier, C., Fan, Q., Wang, X., et al. (2019). Influence of anthropogenic emission inventories on simulations of air quality in China during winter and summer 2010. *Atmospheric Environment*, *198*, 236–256. https://doi.org/10.1016/j.atmosenv.2018.10.043

Brown, S. S., Dubé, W. P., Peischl, J., Ryerson, T. B., Atlas, E., Warneke, C., et al. (2011). Budgets for nocturnal VOC oxidation by nitrate radicals aloft during the 2006 Texas Air Quality Study. *Journal of Geophysical Research*, *116*(D24), D24305. https://doi.org/10.1029/2011JD016544

Cao, H., Fu, T. M., Zhang, L., Henze, D. K., Miller, C. C., Lerot, C., et al. (2018). Adjoint inversion of Chinese non-methane volatile organic compound emissions using space-based observations of formaldehyde and glyoxal. *Atmospheric Chemistry and Physics*, *18*(20), 15017–15046. https://doi.org/10.5194/acp-18-15017-2018

Chaliyakunnel, S., Millet, D. B., & Chen, X. (2019). Constraining emissions of volatile organic compounds over the Indian subcontinent using space-based formaldehyde measurements. *Journal of Geophysical Research: Atmospheres*, *124*(19), 10525–10545. https://doi.org/10.1029/2019JD031262

Chen, D., Li, Q., Stutz, J., Mao, Y., Zhang, L., Pikelnaya, O., et al. (2013). WRF-Chem simulation of NO$_x$ and O$_3$ in the L.A. basin during CalNex-2010. *Atmospheric Environment*, *81*, 421–432. https://doi.org/10.1016/j.atmosenv.2013.08.064

Chen, H., Huang, Y., Shen, H., Chen, Y., Ru, M., Chen, Y., et al. (2016). Modeling temporal variations in global residential energy consumption and pollutant emissions. *Applied Energy*, *184*, 820–829. https://doi.org/10.1016/j.apenergy.2015.10.185

Chen, S. P., Liu, T. H., Chen, T. F., Yang, C. F. O., Wang, J. L., & Chang, J. S. (2010). Diagnostic modeling of PAMS VOC observation. *Environmental Science and Technology*, *44*(12), 4635–4644. https://doi.org/10.1021/es903361r

Chutia, L., Ojha, N., Girach, I. A., Sahu, L. K., Alvarado, L. M. A., Burrows, J. P., et al. (2019). Distribution of volatile organic compounds over Indian subcontinent during winter: WRF-chem simulation versus observations. *Environmental Pollution*, *252*(Pt A), 256–269. https://doi.org/10.1016/j.envpol.2019.05.097

CNEMC. (2013). *China technical specifications for installation and acceptance of ambient air quality continuous automated monitoring system for SO_2, NO_2, O_3 and CO*. (In Chinese). China National Environmental Protection Standard, China Environmental Science Press. Retrieved from http://english.mee.gov.cn/Resources/standards/Air_Environment/air_method/201308/t20130816_257560.shtml

CNEMC. (2018). Chinese ground-based air quality monitoring network [Dataset]. https://doi.org/10.5281/zenodo.7906862

Cuchiara, G. C., Li, X., Carvalho, J., & Rappenglück, B. (2014). Intercomparison of planetary boundary layer parameterization and its impacts on surface ozone concentration in the WRF/Chem model for a case study in Houston/Texas. *Atmospheric Environment*, *96*, 175–185. https://doi.org/10.1016/j.atmosenv.2014.07.013

de Gouw, J. A., Gilman, J. B., Kim, S. W., Lerner, B. M., Isaacman-VanWertz, G., McDonald, B. C., et al. (2017). Chemistry of volatile organic compounds in the Los Angeles basin: Nighttime removal of alkenes and determination of emission ratios. *Journal of Geophysical Research: Atmospheres*, *122*(21), 11843–11861. https://doi.org/10.1002/2017JD027459

Emery, C., Liu, Z., Russell, A. G., Odman, M. T., Yarwood, G., & Kumar, N. (2017). Recommendations on statistics and benchmarks to assess photochemical model performance. *Journal of the Air & Waste Management Association*, *67*(5), 582–598. https://doi.org/10.1080/10962247.2016.1265027

Emery, C., Tai, E., & Yarwood, G. (2001). *Enhanced meteorological modeling and performance evaluation for two Texas ozone episodes*. Final Report Submitted to Texas Natural Resources Conservation Commission. ENVIRON, International Corp.

Enrico, M., Roux, G. L., Marusczak, N., Heimbürger, L. E., Claustres, A., Fu, X., et al. (2016). Atmospheric mercury transfer to peat bogs dominated by gaseous elemental mercury dry deposition. *Environmental Science and Technology*, *50*(5), 2405–2412. https://doi.org/10.1021/acs.est.5b06058

Fang, X., Shao, M., Stohl, A., Zhang, Q., Zheng, J., Guo, H., et al. (2016). Top-down estimates of benzene and toluene emissions in the Pearl River Delta and Hong Kong, China. *Atmospheric Chemistry and Physics*, *16*(5), 3369–3382. https://doi.org/10.5194/acp-16-3369-2016

Friedl, M., & Sulla-Menashe, D. (2015). MCD12C1 MODIS/Terra+Aqua land cover type yearly L3 Global 0.05Deg CMG V006 [Dataset]. NASA EOSDIS Land Processes DAAC. https://doi.org/10.5067/MODIS/MCD12C1.006

Fu, T. M., Jacob, D. J., Palmer, P. I., Chance, K., Wang, Y. X., Barletta, B., et al. (2007). Space-based formaldehyde measurements as constraints on volatile organic compound emissions in east and south Asia and implications for ozone. *Journal of Geophysical Research*, *112*(D6), D06312. https://doi.org/10.1029/2006JD007853

Geng, G., Zhang, Q., Martin, R. V., Lin, J., Huo, H., Zheng, B., et al. (2017). Impact of spatial proxies on the representation of bottom-up emission inventories: A satellite-based analysis. *Atmospheric Chemistry and Physics*, *17*(6), 4131–4145. https://doi.org/10.5194/acp-17-4131-2017

Goldstein, A. H., & Galbally, I. E. (2007). Known and unexplored organic constituents in the Earth's atmosphere. *Environmental Science and Technology*, *41*(5), 1514–1521. https://doi.org/10.1021/es072476p

Guenther, A., Karl, T., Harley, P., Wiedinmyer, C., Palmer, P. I., & Geron, C. (2006). Estimates of global terrestrial isoprene emissions using MEGAN (Model of Emissions of Gases and Aerosols from Nature). *Atmospheric Chemistry and Physics*, *6*(11), 3181–3210. https://doi.org/10.5194/acp-6-3181-2006

Guo, H., Chen, K., Wang, P., Hu, J., Ying, Q., Gao, A., & Zhang, H. (2019). Simulation of summer ozone and its sensitivity to emission changes in China. *Atmospheric Pollution Research*, *10*(5), 1543–1552. https://doi.org/10.1016/j.apr.2019.05.003

Guo, H., Cheng, H. R., Ling, Z. H., Louie, P. K., & Ayoko, G. A. (2011). Which emission sources are responsible for the volatile organic compounds in the atmosphere of Pearl River Delta? *Journal of Hazardous Materials*, *188*(1–3), 116–124. https://doi.org/10.1016/j.jhazmat.2011.01.081

Guo, H., Ling, Z. H., Cheng, H. R., Simpson, I. J., Lyu, X. P., Wang, X. M., et al. (2017). Tropospheric volatile organic compounds in China. *Science of the Total Environment*, *574*, 1021–1043. https://doi.org/10.1016/j.scitotenv.2016.09.116

Guo, H., So, K. L., Simpson, I. J., Barletta, B., Meinardi, S., & Blake, D. R. (2007). C1–C8 volatile organic compounds in the atmosphere of Hong Kong: Overview of atmospheric processing and source apportionment. *Atmospheric Environment*, *41*(7), 1456–1472. https://doi.org/10.1016/j.atmosenv.2006.10.011

Guo, H., Wang, T., Blake, D. R., Simpson, I. J., Kwok, Y. H., & Li, Y. S. (2006). Regional and local contributions to ambient non-methane volatile organic compounds at a polluted rural/coastal site in Pearl River Delta, China. *Atmospheric Environment*, *40*(13), 2345–2359. https://doi.org/10.1016/j.atmosenv.2005.12.011

Guo, J., Miao, Y., Zhang, Y., Liu, H., Li, Z., Zhang, W., et al. (2016). The climatology of planetary boundary layer height in China derived from radiosonde and reanalysis data. *Atmospheric Chemistry and Physics*, *16*(20), 13309–13319. https://doi.org/10.5194/acp-16-13309-2016

He, Z., Wang, X., Ling, Z., Zhao, J., Guo, H., Shao, M., & Wang, Z. (2019). Contributions of different anthropogenic volatile organic compound sources to ozone formation at a receptor site in the Pearl River Delta region and its policy implications. *Atmospheric Chemistry and Physics*, *19*(13), 8801–8816. https://doi.org/10.5194/acp-19-8801-2019

Holzworth, G. C. (1967). Mixing depths, wind speeds and air pollution potential for selected locations in the United States. *Journal of Applied Meteorology and Climatology*, *6*(6), 1039–1044. https://doi.org/10.1175/1520-0450(1967)006<1039:MDWSAA>2.0.CO;2

Hong, C., Zhang, Q., He, K., Guan, D., Li, M., Liu, F., & Zheng, B. (2017). Variations of China's emission estimates: Response to uncertainties in energy statistics. *Atmospheric Chemistry and Physics*, *17*(2), 1227–1239. https://doi.org/10.5194/acp-17-1227-2017

Hsu, Y. K., VanCuren, T., Park, S., Jakober, C., Herner, J., FitzGibbon, M., et al. (2010). Methane emissions inventory verification in southern California. *Atmospheric Environment*, *44*(1), 1–7. https://doi.org/10.1016/j.atmosenv.2009.10.002

Huang, Z., Zhong, Z., Sha, Q., Xu, Y., Zhang, Z., Wu, L., et al. (2021). An updated model-ready emission inventory for Guangdong Province by incorporating big data and mapping onto multiple chemical mechanisms. *Science of the Total Environment*, *769*, 144535. https://doi.org/10.1016/j.scitotenv.2020.144535

Jiang, F., Guo, H., Wang, T. J., Cheng, H. R., Wang, X. M., Simpson, I. J., et al. (2010). An ozone episode in the Pearl River Delta: Field observation and model simulation. *Journal of Geophysical Research*, *115*(D22), D22305. https://doi.org/10.1029/2009jd013583

Jiménez, P. A., González-Rouco, J. F., García-Bustamante, E., Navarro, J., Montávez, J. P., de Arellano, J. V. G., et al. (2010). Surface wind regionalization over complex terrain: Evaluation and Analysis of a high-resolution WRF simulation. *Journal of Applied Meteorology and Climatology*, *49*(2), 268–287. https://doi.org/10.1175/2009jamc2175.1

Karl, T., Guenther, A., Yokelson, R. J., Greenberg, J., Potosnak, M., Blake, D. R., & Artaxo, P. (2007). The tropical forest and fire emissions experiment: Emission, chemistry, and transport of biogenic volatile organic compounds in the lower atmosphere over Amazonia. *Journal of Geophysical Research*, *112*(D18), D18302. https://doi.org/10.1029/2007JD008539

Karl, T., Harley, P., Emmons, L., Thornton, B., Guenther, A., Basu, C., et al. (2010). Efficient atmospheric cleansing of oxidized organic trace gases by vegetation. *Science*, *330*(6005), 816–819. https://doi.org/10.1126/science.1192534

Kim, S. W., McKeen, S. A., Frost, G. J., Lee, S. H., Trainer, M., Richter, A., et al. (2011). Evaluations of NO$_x$ and highly reactive VOC emission inventories in Texas and their implications for ozone plume simulations during the Texas Air Quality Study 2006. *Atmospheric Chemistry and Physics*, *11*(22), 11361–11386. https://doi.org/10.5194/acp-11-11361-2011

Kumar, R., Naja, M., Pfister, G. G., Barth, M. C., Wiedinmyer, C., & Brasseur, G. P. (2012). Simulations over South Asia using the Weather Research and Forecasting model with Chemistry (WRF-Chem): Chemistry evaluation and initial results. *Geoscientific Model Development*, *5*(3), 619–648. https://doi.org/10.5194/gmd-5-619-2012

Li, B., Ho, S. S. H., Li, X., Guo, L., Chen, A., Hu, L., et al. (2021). A comprehensive review on anthropogenic volatile organic compounds (VOCs) emission estimates in China: Comparison and outlook. *Environment International*, *156*, 106710. https://doi.org/10.1016/j.envint.2021.106710

Li, K., Li, J., Tong, S., Wang, W., Huang, R. J., & Ge, M. (2019). Characteristics of wintertime VOCs in suburban and urban Beijing: Concentrations, emission ratios, and festival effects. *Atmospheric Chemistry and Physics*, *19*(12), 8021–8036. https://doi.org/10.5194/acp-19-8021-2019

Li, M., Liu, H., Geng, G., Hong, C., Liu, F., Song, Y., et al. (2017a). Anthropogenic emission inventories in China: A review. *National Science Review*, *4*(6), 834–866. https://doi.org/10.1093/nsr/nwx150

Li, M., Song, Y., Mao, Z., Liu, M., & Huang, X. (2016). Impacts of thermal circulations induced by urbanization on ozone formation in the Pearl River Delta region, China. *Atmospheric Environment*, *127*, 382–392. https://doi.org/10.1016/j.atmosenv.2015.10.075

Li, M., Zhang, Q., Kurokawa, J. i., Woo, J. H., He, K., Lu, Z., et al. (2017b). MIX: A mosaic Asian anthropogenic emission inventory under the international collaboration framework of the MICS-Asia and HTAP. *Atmospheric Chemistry and Physics*, *17*(2), 935–963. https://doi.org/10.5194/acp-17-935-2017

Li, M., Zhang, Q., Streets, D. G., He, K. B., Cheng, Y. F., Emmons, L. K., et al. (2014). Mapping Asian anthropogenic emissions of non-methane volatile organic compounds to multiple chemical mechanisms. *Atmospheric Chemistry and Physics*, *14*(11), 5617–5638. https://doi.org/10.5194/acp-14-5617-2014

Liu, F., Zhang, Q., Tong, D., Zheng, B., Li, M., Huo, H., & He, K. B. (2015). High-resolution inventory of technologies, activities, and emissions of coal-fired power plants in China from 1990 to 2010. *Atmospheric Chemistry and Physics*, *15*(23), 13299–13317. https://doi.org/10.5194/acp-15-13299-2015

Liu, H., Man, H., Cui, H., Wang, Y., Deng, F., Wang, Y., et al. (2017). An updated emission inventory of vehicular VOCs and IVOCs in China. *Atmospheric Chemistry and Physics*, *17*(20), 12709–12724. https://doi.org/10.5194/acp-17-12709-2017

Liu, X., Wang, N., Lyu, X., Zeren, Y., Jiang, F., Wang, X., et al. (2021). Photochemistry of ozone pollution in autumn in Pearl River Estuary, South China. *Science of the Total Environment*, *754*, 141812. https://doi.org/10.1016/j.scitotenv.2020.141812

Liu, Y., Shao, M., Lu, S., Chang, C. C., Wang, J. L., & Fu, L. (2008). Source apportionment of ambient volatile organic compounds in the Pearl River Delta, China: Part II. *Atmospheric Environment*, *42*(25), 6261–6274. https://doi.org/10.1016/j.atmosenv.2008.02.027

Liu, Y., & Wang, T. (2020a). Worsening urban ozone pollution in China from 2013 to 2017 – Part 1: The complex and varying roles of meteorology. *Atmospheric Chemistry and Physics*, *20*(11), 6305–6321. https://doi.org/10.5194/acp-20-6305-2020

Liu, Y., & Wang, T. (2020b). Worsening urban ozone pollution in China from 2013 to 2017 – Part 2: The effects of emission changes and implications for multi-pollutant control. *Atmospheric Chemistry and Physics*, *20*(11), 6323–6337. https://doi.org/10.5194/acp-20-6323-2020

Liu, Z., Wang, Y., Vrekoussis, M., Richter, A., Wittrock, F., Burrows, J. P., et al. (2012). Exploring the missing source of glyoxal (CHOCHO) over China. *Geophysical Research Letters*, *39*(10), L10812. https://doi.org/10.1029/2012GL051645

Louie, P. K. K., Ho, J. W. K., Tsang, R. C. W., Blake, D. R., Lau, A. K. H., Yu, J. Z., et al. (2013). VOCs and OVOCs distribution and control policy implications in Pearl River Delta region, China. *Atmospheric Environment*, *76*, 125–135. https://doi.org/10.1016/j.atmosenv.2012.08.058

Lu, H., Lyu, X., Cheng, H., Ling, Z., & Guo, H. (2019). Overview on the spatial–temporal characteristics of the ozone formation regime in China. *Environmental Science: Processes & Impacts*, *21*(6), 916–929. https://doi.org/10.1039/C9EM00098D

Lu, K., Guo, S., Tan, Z., Wang, H., Shang, D., Liu, Y., et al. (2018). Exploring atmospheric free-radical chemistry in China: The self-cleansing capacity and the formation of secondary air pollution. *National Science Review*, *6*(3), 579–594. https://doi.org/10.1093/nsr/nwy073

Lu, Q., Zheng, J., Ye, S., Shen, X., Yuan, Z., & Yin, S. (2013). Emission trends and source characteristics of SO$_2$, NO$_x$, PM$_{10}$ and VOCs in the Pearl River Delta region from 2000 to 2009. *Atmospheric Environment*, *76*, 11–20. https://doi.org/10.1016/j.atmosenv.2012.10.062

Mar, K. A., Ojha, N., Pozzer, A., & Butler, T. M. (2016). Ozone air quality simulations with WRF-Chem (v3.5.1) over Europe: Model evaluation and chemical mechanism comparison. *Geoscientific Model Development*, *9*(10), 3699–3728. https://doi.org/10.5194/gmd-9-3699-2016

Matsui, H., Koike, M., Kondo, Y., Takegawa, N., Kita, K., Miyazaki, Y., et al. (2009). Spatial and temporal variations of aerosols around Beijing in summer 2006: Model evaluation and source apportionment. *Journal of Geophysical Research*, *114*(D2), D00G13. https://doi.org/10.1029/2008JD010906

MEIC. (2017). 2017-Based multi-resolution emission inventory for China [Dataset]. Retrieved from http://meicmodel.org.cn/?page_id=125&lang=en

Meng, Y., Song, J., Zeng, L., Zhang, Y., Zhao, Y., Liu, X., et al. (2022). Ambient volatile organic compounds at a receptor site in the Pearl River Delta region: Variations, source apportionment and effects on ozone formation. *Journal of Environmental Sciences*, *111*, 104–117. https://doi.org/10.1016/j.jes.2021.02.024

MIX. (2010). 2010-based anthropogenic emission inventory for Asia [Dataset]. Retrieved from http://meicmodel.org.cn/?page_id=87&lang=en

Mo, Z., Huang, S., Yuan, B., Pei, C., Song, Q., Qi, J., et al. (2020). Deriving emission fluxes of volatile organic compounds from tower observation in the Pearl River Delta, China. *Science of the Total Environment*, *741*, 139763. https://doi.org/10.1016/j.scitotenv.2020.139763

Mo, Z., Shao, M., & Lu, S. (2016). Compilation of a source profile database for hydrocarbon and OVOC emissions in China. *Atmospheric Environment*, *143*, 209–217. https://doi.org/10.1016/j.atmosenv.2016.08.025

National Centers for Environmental Prediction (NCEP), National Weather Service, NOAA, & U.S. Department of Commerce. (2000). NCEP FNL operational model global tropospheric analyses, continuing from July 1999. (Updated daily) [Dataset]. Research Data Archive at the National Center for Atmospheric Research, Computational and Information Systems Laboratory. https://doi.org/10.5065/D6M043C6

Nguyen, T. B., Crounse, J. D., Teng, A. P., St. Clair, J. M., Paulot, F., Wolfe, G. M., & Wennberg, P. O. (2015). Rapid deposition of oxidized biogenic compounds to a temperate forest. *Proceedings of the National Academy of Sciences*, *112*(5), E392–E401. https://doi.org/10.1073/pnas.1418702112

NOAA (National Oceanic and Atmospheric Administration). National Centers for Environmental Information. (2001). Global surface hourly Integrated Surface Database (ISD) [Dataset]. NOAA National Centers for Environmental Information. Retrieved from https://www.ncei.noaa.gov/pub/data/noaa/isd-lite/

Parrish, D. D., Stohl, A., Forster, C., Atlas, E. L., Blake, D. R., Goldan, P. D., et al. (2007). Effects of mixing on evolution of hydrocarbon ratios in the troposphere. *Journal of Geophysical Research*, *112*(D10), D10S34. https://doi.org/10.1029/2006JD007583

Qi, J., Mo, Z., Yuan, B., Huang, S., Huangfu, Y., Wang, Z., et al. (2021). An observation approach in evaluation of ozone production to precursor changes during the COVID-19 lockdown. *Atmospheric Environment*, *262*, 118618. https://doi.org/10.1016/j.atmosenv.2021.118618

Qu, H., Wang, Y., Zhang, R., & Li, J. (2020). Extending ozone-precursor relationships in China from peak concentration to peak time. *Journal of Geophysical Research: Atmospheres*, *125*(22), e2020JD033670. https://doi.org/10.1029/2020jd033670

Saikawa, E., Kim, H., Zhong, M., Avramov, A., Zhao, Y., Janssens-Maenhout, G., et al. (2017). Comparison of emissions inventories of anthropogenic air pollutants and greenhouse gases in China. *Atmospheric Chemistry and Physics*, *17*(10), 6393–6421. https://doi.org/10.5194/acp-17-6393-2017

Seinfeld, J. H., & Pandis, S. N. (2006). *Atmospheric chemistry and physics: From air pollution to climate change* (2nd ed.). John Wiley & Sons, Inc.

Shen, L., Jacob, D. J., Zhu, L., Zhang, Q., Zheng, B., Sulprizio, M. P., et al. (2019). The 2005–2016 trends of formaldehyde columns over China observed by satellites: Increasing anthropogenic emissions of volatile organic compounds and decreasing agricultural fire emissions. *Geophysical Research Letters*, *46*(8), 4468–4475. https://doi.org/10.1029/2019gl082172

Simpson, I. J., Blake, N. J., Barletta, B., Diskin, G. S., Fuelberg, H. E., Gorham, K., et al. (2010). Characterization of trace gases measured over Alberta oil sands mining operations: 76 speciated C_2–C_{10} volatile organic compounds (VOCs), CO_2, CH_4, CO, NO, NO_2, NO_y, O_3 and SO_2. *Atmospheric Chemistry and Physics*, *10*(23), 11931–11954. https://doi.org/10.5194/acp-10-11931-2010

Skamarock, W. C., Klemp, J. B., Dudhia, J., Gill, D. O., Liu, Z., Berner, J., et al. (2019). A description of the advanced research WRF Version 4 [Software]. No. NCAR/TN-556+STR. https://doi.org/10.5065/1dfh-6p97

Stavrakou, T., Müller, J. F., Bauwens, M., De Smedt, I., Van Roozendael, M., De Mazière, M., et al. (2015). How consistent are top-down hydrocarbon emissions based on formaldehyde observations from GOME-2 and OMI? *Atmospheric Chemistry and Physics*, *15*(20), 11861–11884. https://doi.org/10.5194/acp-15-11861-2015

Taccone, R. A., Moreno, A., Colmenar, I., Salgado, S., Martín, M. P., & Cabañas, B. (2016). Kinetic study of the OH, NO_3 radicals and Cl atom initiated atmospheric photo-oxidation of iso-propenyl methyl ether. *Atmospheric Environment*, *127*, 80–89. https://doi.org/10.1016/j.atmosenv.2015.12.033

Tang, J. H., Chan, L. Y., Chan, C. Y., Li, Y. S., Chang, C. C., Liu, S. C., et al. (2007). Characteristics and diurnal variations of NMHCs at urban, suburban, and rural sites in the Pearl River Delta and a remote site in South China. *Atmospheric Environment*, *41*(38), 8620–8632. https://doi.org/10.1016/j.atmosenv.2007.07.029

Tuccella, P., Curci, G., Visconti, G., Bessagnet, B., Menut, L., & Park, R. J. (2012). Modeling of gas and aerosol with WRF/Chem over Europe: Evaluation and sensitivity study. *Journal of Geophysical Research*, *117*(D3), D03303. https://doi.org/10.1029/2011jd016302

U.S. EPA. (1999). *Air method, toxic organics-15 (TO-15): Compendium of methods for the determination of toxic organic compounds in ambient air, Second Edition: Determination of volatile organic compounds (VOCs) in air collected in specially-prepared canisters and analyzed by gas chromatography/mass spectrometry (GC/MS)*. EPA 625/R-96/010b. United States Environmental Protection Agency.

U.S. EPA. (2014). CMAQ. (Version 5.0.2) [Software]. https://doi.org/10.5281/zenodo.1079898

Wang, H., Lu, K., Guo, S., Wu, Z., Shang, D., Tan, Z., et al. (2018). Efficient N_2O_5 uptake and NO_3 oxidation in the outflow of urban Beijing. *Atmospheric Chemistry and Physics*, *18*(13), 9705–9721. https://doi.org/10.5194/acp-18-9705-2018

Wang, H., Lyu, X., Guo, H., Wang, Y., Zou, S., Ling, Z., et al. (2018). Ozone pollution around a coastal region of South China Sea: Interaction between marine and continental air. *Atmospheric Chemistry and Physics*, *18*(6), 4277–4295. https://doi.org/10.5194/acp-18-4277-2018

Wang, H., Yan, R., Xu, T., Wang, Y., Wang, Q., Zhang, T., et al. (2020). Observation constrained aromatic emissions in Shanghai, China. *Journal of Geophysical Research: Atmospheres*, *125*(6), e2019JD031815. https://doi.org/10.1029/2019jd031815

Wang, N., Guo, H., Jiang, F., Ling, Z. H., & Wang, T. (2015). Simulation of ozone formation at different elevations in mountainous area of Hong Kong using WRF-CMAQ model. *Science of The Total Environment*, *505*, 939–951. https://doi.org/10.1016/j.scitotenv.2014.10.070

Wang, S., Zheng, J., Fu, F., Yin, S., & Zhong, L. (2011). Development of an emission processing system for the Pearl River Delta Regional air quality modeling using the SMOKE model: Methodology and evaluation. *Atmospheric Environment*, *45*(29), 5079–5089. https://doi.org/10.1016/j.atmosenv.2011.06.037

Wang, T., Xue, L., Brimblecombe, P., Lam, Y. F., Li, L., & Zhang, L. (2017). Ozone pollution in China: A review of concentrations, meteorological influences, chemical precursors, and effects. *Science of the Total Environment*, *575*, 1582–1596. https://doi.org/10.1016/j.scitotenv.2016.10.081

Wang, X., Liang, X. Z., Jiang, W., Tao, Z., Wang, J. X. L., Liu, H., et al. (2010). WRF-Chem simulation of East Asian air quality: Sensitivity to temporal and vertical emissions distributions. *Atmospheric Environment*, *44*(5), 660–669. https://doi.org/10.1016/j.atmosenv.2009.11.011

Warneke, C., de Gouw, J. A., Goldan, P. D., Kuster, W. C., Williams, E. J., Lerner, B. M., et al. (2004). Comparison of daytime and nighttime oxidation of biogenic and anthropogenic VOCs along the New England coast in summer during New England Air Quality Study 2002. *Journal of Geophysical Research*, *109*(D10), D10309. https://doi.org/10.1029/2003JD004424

Wei, W., Li, Y., Wang, Y., Cheng, S., & Wang, L. (2018). Characteristics of VOCs during haze and non-haze days in Beijing, China: Concentration, chemical degradation and regional transport impact. *Atmospheric Environment*, *194*, 134–145. https://doi.org/10.1016/j.atmosenv.2018.09.037

Wesely, M. L. (1989). Parameterization of surface resistances to gaseous dry deposition in regional-scale numerical models. *Atmospheric Environment*, *23*(6), 1293–1304. https://doi.org/10.1016/0004-6981(89)90153-4

Wu, Z., Zhang, L., Walker, J. T., Makar, P. A., Perlinger, J. A., & Wang, X. (2021). Extension of a gaseous dry deposition algorithm to oxidized volatile organic compounds and hydrogen cyanide for application in chemistry transport models. *Geoscientific Model Development*, *14*(8), 5093–5105. https://doi.org/10.5194/gmd-14-5093-2021

Yang, X., Lu, K., Ma, X., Gao, Y., Tan, Z., Wang, H., et al. (2022). Radical chemistry in the Pearl River Delta: Observations and modeling of OH and HO_2 radicals in Shenzhen in 2018. *Atmospheric Chemistry and Physics*, *22*(18), 12525–12542. https://doi.org/10.5194/acp-22-12525-2022

Yarwood, G., Rao, S., Yocke, M., & Whitten, G. (2005). Updates to the carbon bond chemical mechanism: CB05. Final Report to the US EPA, Rep. RT-04-00675.

Yuan, B., Chen, W., Shao, M., Wang, M., Lu, S., Wang, B., et al. (2012). Measurements of ambient hydrocarbons and carbonyls in the Pearl River Delta (PRD), China. *Atmospheric Research*, *116*, 93–104. https://doi.org/10.1016/j.atmosres.2012.03.006

Yuan, B., Kaser, L., Karl, T., Graus, M., Peischl, J., Campos, T. L., et al. (2015). Airborne flux measurements of methane and volatile organic compounds over the Haynesville and Marcellus shale gas production regions. *Journal of Geophysical Research: Atmospheres*, *120*(12), 6271–6289. https://doi.org/10.1002/2015JD023242

Zeren, Y., Guo, H., Lyu, X., Jiang, F., Wang, Y., Liu, X., et al. (2019). An ozone "pool" in South China: Investigations on atmospheric dynamics and photochemical processes over the Pearl River Estuary. *Journal of Geophysical Research: Atmospheres*, *124*(22), 12340–12355. https://doi.org/10.1029/2019jd030833

Zhang, L., Brook, J. R., & Vet, R. (2002). On ozone dry deposition—With emphasis on non-stomatal uptake and wet canopies. *Atmospheric Environment*, *36*(30), 4787–4799. https://doi.org/10.1016/S1352-2310(02)00567-8

Zhang, L., Brook, J. R., & Vet, R. (2003). A revised parameterization for gaseous dry deposition in air-quality models. *Atmospheric Chemistry and Physics*, *3*(6), 2067–2082. https://doi.org/10.5194/acp-3-2067-2003

Zhang, L., He, Z., Wu, Z., Macdonald, A. M., Brook, J. R., & Kharol, S. (2023). A database of modeled gridded dry deposition velocities for 45 gaseous species and three particle size ranges across North America. *Journal of Environmental Sciences*, *127*, 264–272. https://doi.org/10.1016/j.jes.2022.05.030

Zhang, R., Wang, Y., He, Q., Chen, L., Zhang, Y., Qu, H., et al. (2017). Enhanced trans-Himalaya pollution transport to the Tibetan Plateau by cut-off low systems. *Atmospheric Chemistry and Physics*, *17*(4), 3083–3095. https://doi.org/10.5194/acp-17-3083-2017

Zhang, Y., Sartelet, K., Wu, S. Y., & Seigneur, C. (2013). Application of WRF/Chem-MADRID and WRF/Polyphemus in Europe – Part 1: Model description, evaluation of meteorological predictions, and aerosol–meteorology interactions. *Atmospheric Chemistry and Physics*, *13*(14), 6807–6843. https://doi.org/10.5194/acp-13-6807-2013

Zheng, B., Tong, D., Li, M., Liu, F., Hong, C., Geng, G., et al. (2018). Trends in China's anthropogenic emissions since 2010 as the consequence of clean air actions. *Atmospheric Chemistry and Physics*, *18*(19), 14095–14111. https://doi.org/10.5194/acp-18-14095-2018

Zheng, B., Zhang, Q., Tong, D., Chen, C., Hong, C., Li, M., et al. (2017). Resolution dependence of uncertainties in gridded emission inventories: A case study in Hebei, China. *Atmospheric Chemistry and Physics*, *17*(2), 921–933. https://doi.org/10.5194/acp-17-921-2017

Zheng, J., Shao, M., Che, W., Zhang, L., Zhong, L., Zhang, Y., & Streets, D. (2009a). Speciated VOC emission inventory and spatial patterns of ozone formation potential in the Pearl River Delta, China. *Environmental Science and Technology*, *43*(22), 8580–8586. https://doi.org/10.1021/es901688e

Zheng, J., Zhang, L., Che, W., Zheng, Z., & Yin, S. (2009b). A highly resolved temporal and spatial air pollutant emission inventory for the Pearl River Delta region, China and its uncertainty assessment. *Atmospheric Environment*, *43*(32), 5112–5122. https://doi.org/10.1016/j.atmosenv.2009.04.060

Zou, Y., Deng, X. J., Zhu, D., Gong, D. C., Wang, H., Li, F., et al. (2015). Characteristics of 1 year of observational data of VOCs, NO_x and O_3 at a suburban site in Guangzhou, China. *Atmospheric Chemistry and Physics*, *15*(12), 6625–6636. https://doi.org/10.5194/acp-15-6625-2015

References From the Supporting Information

Ang, A. H. S., & Tang, W. H. (1984). *Probability concepts in engineering planning and design, Vol. 2: Decision, risk, and reliability*. John Wiley & Sons Inc.

Carlton, A. G., Bhave, P. V., Napelenok, S. L., Edney, E. O., Sarwar, G., Pinder, R. W., et al. (2010). Model representation of secondary organic aerosol in CMAQv4.7. *Environmental Science and Technology*, *44*(22), 8553–8560. https://doi.org/10.1021/es100636q

Fishman, G. (2013). *Monte Carlo: Concepts, algorithms, and applications* (Illustrated ed.). Springer Science & Business Media.

Helton, J. C. (1994). Treatment of uncertainty in performance assessments for complex systems. *Risk Analysis*, *14*(4), 483–511. https://doi.org/10.1111/j.1539-6924.1994.tb00266.x

Hofzumahaus, A., Rohrer, F., Lu, K., Bohn, B., Brauers, T., Chang, C. C., et al. (2009). Amplified trace gas removal in the troposphere. *Science*, *324*(5935), 1702–1704. https://doi.org/10.1126/science.1164566

Hong, S. Y., Dudhia, J., & Chen, S. H. (2004). A revised approach to ice microphysical processes for the bulk parameterization of clouds and precipitation. *Monthly Weather Review*, *132*(1), 103–120. https://doi.org/10.1175/1520-0493(2004)132<0103:ARATIM>2.0.CO;2

Hong, S. Y., Noh, Y., & Dudhia, J. (2006). A new vertical diffusion package with an explicit treatment of entrainment processes. *Monthly Weather Review*, *134*(9), 2318–2341. https://doi.org/10.1175/mwr3199.1

Jiménez, P. A., Dudhia, J., González-Rouco, J. F., Navarro, J., Montávez, J. P., & García-Bustamante, E. (2012). A revised scheme for the WRF surface layer formulation. *Monthly Weather Review*, *140*(3), 898–918. https://doi.org/10.1175/mwr-d-11-00056.1

Kain, J. S. (2004). The Kain–Fritsch convective parameterization: An update. *Journal of Applied Meteorology*, *43*(1), 170–181. https://doi.org/10.1175/1520-0450(2004)043%3C0170:TKCPAU%3E2.0.CO;2

Kumar, S., Mondal, A. N., Gaikwad, S. A., Devotta, S., & Singh, R. N. (2004). Qualitative assessment of methane emission inventory from municipal solid waste disposal sites: A case study. *Atmospheric Environment*, *38*(29), 4921–4929. https://doi.org/10.1016/j.atmosenv.2004.05.052

Li, S., Liu, W., Xie, P., Qin, M., & Yang, Y. (2012). Observation of nitrate radical in the nocturnal boundary layer during a summer field campaign in Pearl River Delta, China. *Terrestrial, Atmospheric and Oceanic Sciences*, *23*(1), 39–48. https://doi.org/10.3319/TAO.2011.07.26.01(A)

Lu, K. D., Rohrer, F., Holland, F., Fuchs, H., Bohn, B., Brauers, T., et al. (2012). Observation and modelling of OH and HO_2 concentrations in the Pearl River Delta 2006: A missing OH source in a VOC rich atmosphere. *Atmospheric Chemistry and Physics*, *12*(3), 1541–1569. https://doi.org/10.5194/acp-12-1541-2012

Mlawer, E. J., Taubman, S. J., Brown, P. D., Iacono, M. J., & Clough, S. A. (1997). Radiative transfer for inhomogeneous atmospheres: RRTM, a validated correlated-k model for the longwave. *Journal of Geophysical Research*, *102*(D14), 16663–16682. https://doi.org/10.1029/97JD00237

Tan, Z., Lu, K., Hofzumahaus, A., Fuchs, H., Bohn, B., Holland, F., et al. (2019). Experimental budgets of OH, HO_2, and RO_2 radicals and implications for ozone formation in the Pearl River Delta in China 2014. *Atmospheric Chemistry and Physics*, *19*(10), 7129–7150. https://doi.org/10.5194/acp-19-7129-2019

Tewari, M., Chen, F., Wang, W., Dudhia, J., LeMone, M., Mitchell, K., et al. (2004). Implementation and verification of the unified NOAH land surface model in the WRF model. In *Paper presented at the 20th conference on weather analysis and forecasting/16th conference on numerical weather prediction*.

Wang, H., Chen, J., & Lu, K. (2015). Measurement of NO_3 and N_2O_5 in the troposphere. *Progress in Chemistry*, *27*(7), 963. https://doi.org/10.7536/PC141230

Wayne, R. P., Barnes, I., Biggs, P., Burrows, J. P., Canosa-Mas, C. E., Hjorth, J., et al. (1991). The nitrate radical: Physics, chemistry, and the atmosphere. *Atmospheric Environment, Part A: General Topics*, *25*(1), 1–203. https://doi.org/10.1016/0960-1686(91)90192-A

Yan, C., Tham, Y. J., Zha, Q., Wang, X., Xue, L., Dai, J., et al. (2019). Fast heterogeneous loss of N_2O_5 leads to significant nighttime NO_x removal and nitrate aerosol formation at a coastal background environment of southern China. *Science of the Total Environment*, *677*, 637–647. https://doi.org/10.1016/j.scitotenv.2019.04.389

Zhang, Y., Wang, X., Barletta, B., Simpson, I. J., Blake, D. R., Fu, X., et al. (2013). Source attributions of hazardous aromatic hydrocarbons in urban, suburban and rural areas in the Pearl River Delta (PRD) region. *Journal of Hazardous Materials*, *250–251*, 403–411. https://doi.org/10.1016/j.jhazmat.2013.02.023

Zhao, Y., Nielsen, C. P., Lei, Y., McElroy, M. B., & Hao, J. (2011). Quantifying the uncertainties of a bottom-up emission inventory of anthropogenic atmospheric pollutants in China. *Atmospheric Chemistry and Physics*, *11*(5), 2295–2308. https://doi.org/10.5194/acp-11-2295-2011